Journal of Inorganic Biochemistry 227 (2022) 111689

Contents lists available at ScienceDirect

Journal of Inorganic Biochemistry

journal homepage: www.elsevier.com/locate/jinorgbio

Impact of the dynamics of the catalytic arginine on nitrite and chlorite binding by dimeric chlorite dismutase

Ilenia Serra [a,1], Daniel Schmidt [b,1], Vera Pfanzagl [b], Georg Mlynek [c,d], Stefan Hofbauer [b], Kristina Djinović-Carugo [d,e], Paul G. Furtmüller [b], Inés García-Rubio [f,g], Sabine Van Doorslaer [a], Christian Obinger [b,*]

[a] BIMEF Laboratory, Department of Chemistry, University of Antwerp, Belgium
[b] Department of Chemistry, Institute of Biochemistry, University of Natural Resources and Life Sciences, Vienna, Muthgasse 18, A-1190 Vienna, Austria
[c] Core Facility Biomolecular & Cellular Analysis, University of Natural Resources and Life Sciences, Vienna, Muthgasse 11, A-1190 Vienna, Austria
[d] Department of Structural and Computational Biology, Max Perutz Laboratories, A-1030, Vienna, Austria
[e] Department of Biochemistry, Faculty of Chemistry and Chemical Technology, University of Ljubljana, Večna pot 5, SI-1000 Ljubljana, Slovenia
[f] Department of Condensed Matter Physics, Faculty of Sciences, University of Zaragoza, 50009 Zaragoza, Spain
[g] Centro Universitario de la Defensa, 50090 Zaragoza, Spain

ARTICLE INFO

Keywords:
Chlorite dismutase
Catalytic arginine
Substrate adduct
X-ray crystallography
electron paramagnetic resonance
Molecular dynamics simulation

ABSTRACT

Chlorite dismutases (Clds) are heme *b* containing oxidoreductases able to decompose chlorite to chloride and molecular oxygen. This work analyses the impact of the distal, flexible and catalytic arginine on the binding of anionic angulate ligands like nitrite and the substrate chlorite. Dimeric Cld from *Cyanothece* sp. PCC7425 was used as a model enzyme. We have investigated wild-type *C*Cld having the distal catalytic R127 hydrogen-bonded to glutamine Q74 and variants with R127 (i) being arrested in a salt-bridge with a glutamate (Q74E), (ii) being fully flexible (Q74V) or (iii) substituted by either alanine (R127A) or lysine (R127K). We present the electronic and spectral signatures of the high-spin ferric proteins and the corresponding low-spin nitrite complexes elucidated by UV–visible, circular dichroism and electron paramagnetic resonance spectroscopies. Furthermore, we demonstrate the impact of the dynamics of R127 on the thermal stability of the respective nitrite adducts and present the X-ray crystal structures of the nitrite complexes of wild-type *C*Cld and the variants Q74V, Q74E and R127A. In addition, the molecular dynamics (MD) and the binding *modi* of nitrite and chlorite to the ferric wild-type enzyme and the mutant proteins and the interaction of the oxoanions with R127 have been analysed by MD simulations. The findings are discussed with respect to the role(s) of R127 in ligand and chlorite binding and substrate degradation.

1. Introduction

Chlorite dismutases (Clds, EC 1.13.11.49) are heme *b*-containing prokaryotic oxidoreductases [1,2], which belong to the structural superfamily of porphyrin-binding dimeric α + β barrel proteins that typically show a high functional diversity [3,4]. Clds convert chlorite (ClO_2^-) to chloride (Cl^-) and dioxygen (O_2). These heme enzymes attracted attention because of (i) their ability to catalyze O-O bond formation and (ii) their potential application in the bioremediation of harmful anthropogenic chlorite present in groundwater, drinking water, and soil [1,2].

The reaction mechanism of Clds is still debated, as is the role of the flexible catalytic arginine, which is the only charged amino acid in an otherwise hydrophobic distal heme cavity [1,2]. Clds convert chlorite in three steps (Reactions 1, 3, 4) in which the catalytic arginine might be involved. The reaction is initiated by the binding of negatively charged

Abbreviations: Cld, chlorite dismutase; *C*Cld, chlorite dismutase from *Cyanothece* sp. PCC7425; CW, continuous wave; *D*, tetragonal zero-field splitting; DSC, differential circular calorimetry; *E*, rhombic zero-field splitting; ECD, electronic circular dichroism; EPR, electron paramagnetic resonance; HS, high-spin; LS, low-spin; *Nd*Cld, chlorite dismutase from "*Candidatus* Nitrospira defluvii"; WT, wild type; ZFS, zero-field splitting.

* Corresponding author.
E-mail address: christian.obinger@boku.ac.at (C. Obinger).

[1] Both authors contributed equally to this manuscript

https://doi.org/10.1016/j.jinorgbio.2021.111689
Received 28 September 2021; Received in revised form 15 November 2021; Accepted 3 December 2021
Available online 10 December 2021
0162-0134/© 2021 Published by Elsevier Inc.

chlorite [pK_a (chlorous acid) = 1.96; bond angle 111°; electronegativity (Cl) = 3.16] to the ferric state of Cld thereby forming the substrate adduct (Reaction 1). Similar to chlorite, nitrite is also an angulate oxoanion of the same formal charge at neutral pH and very similar bond angle [pK_a (nitrous acid) = 3.15; bond angle 115°, electronegativity (N) = 3.04] that forms a low-spin (LS) complex with the ferric Cld (Reaction 2). The latter mirrors the substrate adduct in Reaction 1.

The substrate adduct cannot be trapped in Clds since chlorite is a strong oxidant that immediately oxidizes the ferric enzyme to an oxoiron (IV) intermediate, either Compound I [Por$^{\bullet+}$Fe(IV) = O] or Compound II [PorFe(IV) = O]. As a consequence, chlorite is either reduced to hypochlorite ($^{-}$OCl) (Reaction 3a) or chlorine monoxide ($^{\bullet}$OCl) (Reaction 3b). The actual molecular mechanism is still under discussion [5–18]. Finally, the transient chlorite reduction products must rearrange before rebinding to and reacting with the respective oxoiron(IV) intermediate to release dioxygen and chloride (Reactions 4a or 4b).

$$[\mathrm{PorFe(III)}]^{+} + [\mathrm{O-Cl-O}]^{-} \rightarrow [\mathrm{PorFe(III)}]^{+} - [\mathrm{O-Cl-O}]^{-} \quad \text{Reaction 1}$$

$$[\mathrm{PorFe(III)}]^{+} + [\mathrm{O-N-O}]^{-} \rightarrow [\mathrm{PorFe(III)}]^{+} - [\mathrm{O-N-O}]^{-} \quad \text{Reaction 2}$$

$$[\mathrm{PorFe(III)}]^{+} - [\mathrm{O-Cl-O}]^{-} \rightarrow [\mathrm{Por^{\bullet+}Fe(IV)=O}]^{+} + \mathrm{ClO}^{-} \quad \text{Reaction 3a}$$

$$[\mathrm{PorFe(III)}]^{+} - [\mathrm{O-Cl-O}]^{-} \rightarrow [\mathrm{PorFe(IV)=O}] + \mathrm{ClO}^{\bullet} \quad \text{Reaction 3b}$$

$$[\mathrm{Por^{\bullet+}Fe(IV)=O}]^{+} \ldots {}^{-}\mathrm{OCl} \rightarrow [\mathrm{PorFe(III)}]^{+} + \mathrm{O_2} + \mathrm{Cl}^{-} \quad \text{Reaction 4a}$$

$$[\mathrm{PorFe(IV)=O}] \ldots {}^{\bullet}\mathrm{OCl} \rightarrow [\mathrm{PorFe(III)}]^{+} + \mathrm{O_2} + \mathrm{Cl}^{-} \quad \text{Reaction 4b}$$

Phylogenetic analysis demonstrated the presence of two Cld clades [1,2], which differ in oligomeric state as well as overall sequence length and architecture of the subunits. Typically, clade 1 Clds are homopenta- or homohexamers with "long" subunits consisting of two ferredoxin-like folds [5–8,10–14], whereas clade 2 Clds are homodimers with "short" subunits, which are lacking most of the N-terminal ferredoxin-like fold [9,15–18]. However, the C-terminal heme-binding ferredoxin-like fold is highly similar to that of clade 1 Clds.

In the ferric resting state, the heme iron of Clds is ligated by a proximal histidine and all so far published crystal structures show the presence of a distal water [15]. As mentioned above, the only charged amino acid in the hydrophobic distal heme cavity is a fully conserved catalytic arginine (R127 in chlorite dismutase from *Cyanothece* sp. PCC7425, *i.e. C*Cld), which is flexible and switches between two conformations, *i.e.* toward either the heme iron ("in") or the substrate entry channel ("out") [4,5,7–14,17,18]. Interestingly, the hydrogen-bonding network of this arginine is different in clade 1 and clade 2 Clds. Despite sharing the same heme cavity architecture, which is reflected by similar redox properties and chlorite degradation activities [1,2,10], in clade 2 Clds the catalytic arginine is H-bonded to a glutamine, whereas in clade 1 Clds it does not interact with neighboring amino acids [18]. Recently, this structural difference between clade 1 and clade 2 Clds was mirrored by the design of the *C*Cld variant Q74V that reflects the situation in clade 1 Clds. In addition, the variant Q74E was produced to fix R127 in a salt-bridge and diminish its flexibility [18]. It has been demonstrated that the conformational dynamics of R127 has a significant role in heme coordination during alkaline transition and in the thermal stability of the heme cavity [18]. Moreover, the K_M value for chlorite, calculated for the overall reaction, inversely correlated with the flexibility of R127, *i.e.* K_M (Q74V) < K_M (wild-type *C*Cld) < K_M (Q74E) at pH 5.0 and neutral pH, whereas the impact on the overall catalytic efficiency was relatively small [18].

Here, in order to get more insight into the role of the flexible catalytic arginine and its role(s) in substrate binding and degradation, we investigated its involvement in the formation of the substrate adduct (Reaction 1) mirrored by the formation of the LS nitrite complex (Reaction 2). We present the electronic and spectral signatures of the high-spin ferric proteins and the corresponding low-spin nitrite complexes elucidated by UV–vis, circular dichroism and electron paramagnetic resonance (EPR) spectroscopies. Furthermore, we demonstrate the impact of the dynamics of R127 on the thermal stability of the respective nitrite adducts and present the X-ray crystal structures of the nitrite complexes of wild-type *C*Cld and the variants Q74V, Q74E and R127A. Additionally, molecular dynamics (MD) of the active site along with ligand binding to the Fe(III) of wild-type and variant proteins and the interactions with R127 have been analysed by MD simulations. This work clearly shows that (i) the flexibility of the catalytic arginine has a strong impact on the thermodynamics of binding of angulate oxoanions and (ii) chlorite and nitrite exhibit different binding *modi* to the ferric resting state of Cld.

2. Materials and methods

2.1. Site-directed mutagenesis, expression and purification

The *C*Cld variants R127A and R127K were obtained by site-directed mutagenesis using the QuikChange Lightning Kit (Agilent, Santa Clara, CA, USA). The modified wild-type plasmid described previously [18] was used as template (Table S1). For control, the final plasmid was sequenced from the primer pET-up (Microsynth, Balgach, Switzerland).

Recombinant protein expression of *C*Cld variants was performed in *E. coli* BL21 Gold (DE3) cells (Agilent) in LB-medium supplemented with ampicillin as recently reported [18]. For protein purification the cell pellets were thawed and resuspended in lysis buffer (50 mM phosphate buffer, pH 7.4, 500 mM NaCl, 0.5% Triton X-100 and 5% glycerol) and supplemented with ~100 μM hemin. After ultrasonication (two 3 min-cycles, pulsed mode, 1 s sonication, 1 s rest, 90%) on ice, the cell lysate was centrifuged (4 °C, 17000 *g*, 35 min). Following a filtration step (0.45 μm, Durapore Membrane, Merck, Darmstadt, Germany) the resulting crude extract was loaded onto a His-trap affinity column (5 mL; GE Healthcare, Chicago, IL, USA) pre-equilibrated with binding buffer (50 mM phosphate buffer, pH 7.4, 500 mM NaCl). After the protein-loaded column was washed with binding buffer, on-column cleavage of the His-tag was performed. Therefore, the column was equilibrated with cleavage buffer (50 mM Tris-HCl with 150 mM NaCl and 1 mM EDTA) and cleaving with a His-tagged HRV 3C PreScission Protease was performed overnight at 4 °C. Elution was carried out with storage buffer (50 mM phosphate buffer, pH 7.0) accompanied by a concentration and desalting step using an Amicon Ultra-15 centrifugal filter unit (10 kDa molecular weight cut-off; Merck, Darmstadt, Germany). As a final polishing step, the concentrated protein was applied to a pre-equilibrated (50 mM phosphate buffer, pH 7.0) HiLoad 16/60 Superdex 200 prep grade column (GE Healthcare). The collected fractions were pooled, concentrated to a concentration of ~20 mg mL^{-1} using centrifugal filter unit and stored at −80 °C in 50–100 μL aliquots.

2.2. UV–visible and electronic circular dichroism spectroscopy

UV–visible spectra (200–800 nm) were recorded routinely using a Cary 60 UV–vis spectrophotometer (Agilent) at 25 °C. For determination of enzyme concentration, a molar extinction coefficient of heme of ϵ_{Soret} = 100,000 M^{-1} cm^{-1} was used [18]. For determination of K_D of the Cld-nitrite complex, 10 μM enzyme in 50 mM phosphate-citrate buffer (pH 5.0), phosphate buffer (pH 7.0) or phosphate-borate buffer (pH 9.0) were titrated step by step with the low-spin (LS) ligand. From the resulting difference spectra specific wavelengths at 400 nm, 408 nm, 420 nm, 500 nm, 510 nm, 532 nm, 570 nm and 608 nm, depending on the variant, have been selected for plotting ΔAbs *versus* nitrite concentration. Sigma plot (Version 13.0, Systat Software, San Jose, CA, USA) was used to fit the resulting curves to the following hyperbola equation with *b* corresponding to K_D, *x* representing the nitrite concentration, *a* corresponding to the maximal absorption of the Soret band in saturation of the ligand and *y* being the absorption at the respective wavelength:

$$y = \frac{ax}{b + x}$$

For electronic circular dichroism spectroscopy, Chirascan from Applied Photophysics (Leatherhead, UK) was used. Spectra were recorded in the far-UV region (180–260 nm) and in the visible region (260–500 nm) using 10 μM *C*Cld. The path lengths for the far-UV and visible region were 1 mm and 10 mm, respectively. Used buffers were 5 mM citrate-phosphate buffer (pH 5.0), 5 mM phosphate buffer (pH 7.0) and 5 mM borate-phosphate buffer (pH 9.0). The spectral bandwidth was set to 1 mm and the scan speed was 5 s nm^{-1}.

2.3. Electron paramagnetic resonance spectroscopy and crystal field analysis

The effects of the addition of a large excess of $NaNO_2$ to wild-type ferric *C*Cld and variants were assessed by electron paramagnetic resonance (EPR) spectroscopy. In addition, measurements of ferric *Nd*Cld and myoglobin in presence of nitrite were performed as well. EPR samples of chlorite dismutases were prepared taking care of consistency with the other experiments presented in this work. More specifically, for measurements at neutral pH *C*Cld samples were either prepared in 50 mM sodium-phosphate buffer (sodium phosphate monobasic-dibasic mixture), pH 7.0 (R127A, R127K) or in a 50 mM "temperature-independent" (TIP) buffer, pH 7.0, composed of 45% HEPES and 55% sodium phosphate [19] (NO_2^- complex of wild-type *C*Cld). *Nd*Cld samples were prepared in 50 mM HEPES buffer, pH 7.0 (storage buffer following protein purification [12]). Myoglobin from equine skeletal muscle (HsMb) (95–100% pure, essentially salt-free, lyophilized powder) was purchased from Sigma-Aldrich and used without further purification. HsMb samples were prepared in 50 mM Tris-HCl buffer, pH 7.0. For measurements at basic pH, samples of NO_2^- complexes of Q74E and Q74V were prepared either in 50 mM phosphate/borate buffer, pH 8.5, or in 50 mM Tris-HCl, pH 8.5 (both buffers were filtered and degassed before use). Where not otherwise specified, protein concentration was 400 μM and $NaNO_2$ was added in a 500-fold excess (final concentration of 200 mM). Samples of nitrite adducts for EPR experiments were freshly prepared before each measurement to avoid possible effects due to the high concentration of nitrite and interference of NO, which can be formed at acidic pH (see Discussion section) [49]. In particular, the following procedure was used: first, the appropriate volumes of protein stock solution and buffer were mixed together in a standard 1.5 mL -Eppendorf tube to obtain the correct dilution; next, an aliquot of a concentrated $NaNO_2$ solution was added to the mixture to get the desired protein:NO_2^- ratio. The sample was then quickly transferred in an EPR tube (Ø = 4 mm) and immediately frozen in liquid N_2.

X-band continuous wave (CW)-EPR measurements of *C*Cld and *Nd*Cld samples at pH 7.0 (with and without $NaNO_2$) were performed on a Bruker ESP300E spectrometer operating at microwave frequencies of ~9.44 GHz. Temperature was set to 10 K with the use of a liquid-helium cryostat (Oxford Inc.) and excess of paramagnetic O_2 was removed by applying several freeze-pump-thaw cycles to the quartz EPR tubes containing the samples, before starting the EPR experiment. Measurements of NO_2^- complexes of Q74E and Q74V at pH 8.5 and HsMb were carried out with a Bruker ELEXSYS E580 X-band spectrometer equipped with an Oxford ESR 900 continuous-flow helium cryostat and a Bruker ER 4122 SHQ resonator (operating at a microwave frequency of ~9.4 GHz). Spectra were recorded at 10 K under non-saturating conditions. In particular, the microwave power was adjusted in each experiment according to protein concentration or resonator sensitivity in order to obtain non-saturated spectra. A modulation frequency of 100 kHz and a modulation amplitude of 1 mT were also used. Simulations of EPR parameters were performed with the EasySpin tool (v. 6.0.0-dev.26) [20].

The EPR spectra of the low-spin NO_2^- complexes of chlorite dismutases and reference heme proteins were further analysed with a crystal-field model, which allows to correlate the *g*-values obtained from the simulations to the energy differences of the iron t_{2g} orbitals [21–23]. The rhombic (V/λ) and the tetragonal (Δ/λ) crystal field parameters were calculated according to Taylor's formalism [24] using the following relations, where V is defined as the energy splitting between the d_{xz} and d_{yz} orbitals, Δ as the splitting between the d_{xy} and the average of the energy levels of the d_{xz} and d_{yz} orbitals and λ as the spin-orbit coupling factor (see energy scheme in Fig. S11):

$$A = \frac{g_x}{g_z + g_y} + \frac{g_y}{g_z - g_x} = V \Big/ \lambda \quad (1)$$

$$B = \frac{g_x}{g_z + g_y} + \frac{g_z}{g_y - g_x} \quad (2)$$

$$\Delta/\lambda = B - A/2 \quad (3)$$

A "Blumberg-Peisach" diagram [25] (Fig. S12) was constructed by plotting the rhombicity (V/Δ), which reflects the relative rhombic-to-axial character of the system, *versus* the tetragonal field parameter (Δ/λ) for each low-spin species.

2.4. Chlorite degradation activity

Enzyme-mediated chlorite degradation was measured polarographically following the release of O_2 by using a Clark-type oxygen electrode (Oxygraph Plus; Hansatech Instruments, Norfolk, UK). Reactions were monitored at 30 °C using a connected water bath. The electrode was calibrated by equilibrating to 100% O_2 air by bubbling with air and to 0% O_2 saturation by flushing with N_2 until stable plateaus were reached to derive an offset and calibration factor. Reactions were performed in O_2-free 50 mM phosphate buffer, pH 7.0. Substrate was added to final concentrations of $NaClO_2$ ranging from 250 μM to 50 mM. Concentrations of the chlorite stock solutions were determined by using its molar extinction coefficient at 260 nm, *i.e.* 154 M^{-1} cm^{-1} [26]. Reactions were started by adding 20 nM (wild-type *C*Cld, Q74V, Q74E) or 250 nM enzyme (R127A and R127K). Finally, dioxygen production rates (μM O_2 s^{-1}) were determined from the initial linear time traces and plotted *versus* chlorite concentration to derive catalytic parameters.

2.5. Differential scanning calorimetry

Differential scanning calorimetric (DSC) experiments were performed on a MicroCal PEAQ-DSC Automated (Malvern Panalytical Ltd., Malvern, UK) equipped with an autosampler for 96 well plates and controlled by the MicroCal PEAQ-DSC software (cell volume: 130 μL). Samples were analysed over a temperature range of 20 to 80 °C, using a heating scan rate of 60 °C h^{-1}. Each sample was immediately rescanned to check for reversible unfolding. Furthermore, if no refolding was detectable, this rescan was used as baseline. Wild-type *C*Cld and variants were applied as 20 μM solution in 50 mM citrate phosphate buffer (pH 5.0), phosphate buffer (pH 7.0) and borate phosphate buffer (pH 9.0). For LS complex formation 20 mM, 100 mM and 200 mM sodium nitrite ($NaNO_2$) was added to the ferric proteins, at pH 5.0, 7.0 and 9.0 respectively. Fitting of the data was performed with the MicroCal PEAQ-DSC software using a non-two-state equilibrium unfolding model.

2.6. X-ray crystallography

Crystallization experiments were performed using the sitting drop vapor diffusion method in SWISSCI MRC three-well crystallization plates (Molecular Dimensions, Newmarket, UK). Crystallization drops were set up using a mosquito crystallization robot (TTP Labtech, GB). The reservoir was filled with 40 μL precipitant solution. In the sample wells, ratios of 150:200 nL, 200:200 nL, and 250:200 nL protein to precipitant were dispensed. Protein concentration was approximately 10 mg mL^{-1} in 50 mM phosphate buffer, pH 7.0. In addition to known

crystallization conditions [17,18], 0.1 M MES, pH 6.5, 0.15 M $MgSO_4$, 28% *w/v* polyethylene glycol 3350, 3% *v*/v glycerol (for wild-type *C*Cld and Q74E) and 0.1 M TRIS, pH 8.5, 0.2 M $MgCl_2$, 20 w/v% PEG 8000 (for Q74V) were used. Commercially available crystallization screens were used for further screening for the other *C*Cld variants (R127A and R127K). Crystallization plates were stored in a Formulatrix RI-1000 imaging device at 22 °C. Successful hits were obtained using the known conditions (wild-type *C*Cld, Q74V and Q74E, R127A (for soaked crystals) and R127K) and the PACT premier screen from Molecular Dimensions (R127A). Initial screening conditions were optimized for growth of larger crystals by using the micro seeding technique. For this method, a single crystal was placed in crystallization solution in a fresh tube and crushed by vortexing using the Seed Bead™ kit (Hampton Research, Aliso Viejo, CA, USA). The seeding solution was used in a ratio of 1:100 for further crystallization. Final conditions were as follows. For wild-type *C*Cld-nitrite complex: 0.1 M MES pH 6.5, 0.15 M $MgSO_4$, 24% *w/v* PEG 3350; Q74V-nitrite complex: 20% w/v PEG 8000, 0.1 M TRIS pH 8.5, 0.2 M $MgCl_2$; Q74E-nitrite complex: 0.1 M MES pH 6.5, 0.15 M $MgSO_4$, 23% w/v PEG 3350, 2% *v*/v Glycerol; R127A: 0.1 M TRIS pH 8, 20% w/v PEG 6000, 0.2 M $MgCl_2$; R127A-nitrite complex: 0.1 M MES pH 6.5, 0.15 M $MgSO_4$, 23% w/v PEG 3350, 5% v/v glycerol; R127K: 0.1 M MES pH 6.5, 0.15 M $MgSO_4$, 30% w/v PEG 3350, 4% v/v glycerol. All crystals were soaked with mother liquor supplemented with 20% glycerol, except R127A, which was supplemented with 20% 2-methyl-2,4-pentanediol (MPD). Crystals were harvested using a cryo-loop and, finally, flash-vitrified in liquid nitrogen.

Data sets of the variants R127A and R127K were collected at 100 K using an Eiger2 XE 16 M detector at the beamline i04 at the Diamond Light Source (DLS, Didcot, United Kingdom). Further data was collected at 100 K at beamline ID30A-3 (wild-type *C*Cld-nitrite complex) using a Eiger X 4 M detector, at beamline ID-23-1 (nitrite complexes of Q74V and Q74E) using a Pilatus 6 M detector and at beamline ID23-2 (R127A-nitrite complex) using a PILATUS3 X 2 M detector at the of European Synchrotron Radiation Facility (ESRF, Grenoble, France).

Datasets were processed with XDS and symmetry equivalent reflections were merged with XDSCONV [27]. Intensities were not converted to amplitudes. Initially we used a conservative high-resolution cutoff I/SIGMA = 1–2 [28]. The phase problem was solved by molecular replacement using phenix.phaser [29] taken the search models 5MAU, 7ASB and 7ATI [18]. The model was further improved by iterative cycles of manual model building using COOT [30] and maximum likelihood refinement using phenix.refine [31]. Phenix.refine converted intensities into amplitudes using the French and Wilson algorithm [32]. B-factor model was selected using the algorithm implemented in PDB_REDO, which is based on the number of X-ray reflections per atom and a recent implementation of the Hamilton test [33–35]. The final high-resolution cut-off was based on performing paired refinement using the PDB_REDO webserver [36]. Final stages of refinement included either Translation Liberation Screw (TLS) parameters, isotropic or anisotropic B-factor models, automated addition of hydrogens and water molecules, optimization of X-ray/ADP weight, and optimization of X-ray/stereochemistry weight. The model was validated with MolProbity [37]. Figures were prepared with PyMOL Molecular Graphics System (Version 2.3.4, Schrödinger, LLC). The PyMOL-Plugin CAVER 3.0 [38] was used to characterize changes in the active site channel due to introduced mutations. Starting point for channel calculations was the heme iron in the active site.

2.7. Molecular dynamic simulations

All molecular dynamics simulations of *C*Cld were started based on the respective crystal structures of the resting state [PBD code: 5MAU (wild-type *C*Cld), 7ATI (Q74V) and 7ASB (Q74E)] and were performed using the GROMOS11 molecular simulation package [39] and GROMOS force field 54A8 [40]. The heme *b* cofactor was linked to the coordinating histidine [41] and the structures were relaxed by an *in-vacuo* steepest descent energy minimization with a convergence criterion of 0.1 kJ/mol [42]. The relaxed structures were solvated in a periodic rectangular simulation box with the simple point charge water model [43] (minimal solute-wall distance of 0.8 nm), followed by a second energy minimization step to remove unfavourable solute-solvent contacts. To obtain a neutral system and mimic a 50 mM buffer, pH 7, 30 sodium and 24 chloride ions were added to the system prior to equilibration (gradual temperature increases of 60 K every 20 ps followed by 100 ps with $T = 300$ K, constant pressure). Parameters for chlorite were taken from Sündermann et al. 2014 [13]. For nitrite parameters were calculated using the automated topology builder webserver (https://atb.uq.edu.au/). For simulations with nitrite or chlorite in the active site ("bound form") the water molecules directly above the heme iron were manually replaced with nitrite before the second energy minimization and relaxed together with the solvent.

Plain MD simulations ($T = 300$ K, $p = 1$ atm) were performed for 50 ns using a step size of 2 fs. Coordinates were written out every 0.5 ps. This was achieved through weak coupling with a relaxation time of 0.1 ps for the temperature and 0.5 ps for the pressure [44]. The isothermal compressibility was set to 4.575×10^{-4} (kJ mol $nm^{-3})^{-1}$. Bond lengths were constrained to their optimal values with a relative geometric accuracy of 10^{-4} using the SHAKE algorithm [45]. The non-bonding interactions were calculated using a twin-range cut-off [46] and a molecular pair list, with a short-range cut-off of 8 nm and a long-range cut-off of 1.4 nm. A reaction-field contribution [47] was added to the electrostatic interactions and forces to account for a homogeneous medium outside the cut-off using a dielectric permittivity of 61 [48]. Analyses of the coordinate trajectories was done with Gromos++ programs *hbond*, *rdf* and *mdf*. Coordinates at specific time point were generated using Gromos++ program *frameout* and analysed using PyMOL Molecular Graphics System (Version 2.3.4, Schrödinger, LLC).

2.8. Data availability

The structures presented in this paper have all been deposited in the Protein Data Bank (PDB) with the following codes: 7OWI (R127A), 7OUA (R127K), 7OU5 (wild-type *C*Cld soaked with NO_2^-), 7OU9 (Q74E soaked with NO_2^-), 7OU7 (Q74V soaked with NO_2^-) and 7OUY (R127A soaked with NO_2^-). All remaining data are contained within the article.

3. Results

3.1. Electronic configuration of ferric wild-type CCld and variants and the corresponding low-spin nitrite complexes

The far-UV Electronic Circular Dichroism (ECD) spectra (200–260 nm) of recombinant wild-type *C*Cld and the investigated variants Q74A, Q74E, R127A and R127K are very similar, suggesting that the overall secondary structure has not been altered by the inserted mutations (Fig. S1B) [18]. Increasing the pH from 5 to 9 had no impact on the spectral characteristics in the far-UV region (Fig. S1B). At pH 9, changes in the visible ECD spectra of wild-type *C*Cld and the R127A variant indicate the formation of a hydroxo-low-spin (LS), as previously reported for other *C*Cld variants [18]. This distinct shift is not visible for the R127K variant (Fig. S1A).

At pH 5.0 in the visible region, wild-type *C*Cld and the variants Q74V and Q74E show absorption spectra characteristic of the ferric high-spin (HS) states (Figs. 1 & S2) [18]. Wild-type *C*Cld exhibits a Soret band at 405 nm, Q-bands at 510, 531, and 570 nm, and a charge transfer band (CT) at 630 nm (Fig. 1). In the Q-band and CT-band region both Q74V and Q74E show some deviations from the wild-type spectrum. However, addition of nitrite diminishes these differences and similar low-spin complex spectra of these three proteins were obtained, characterized by a red-shifted Soret band at 414 nm, Q-bands at 531–536 nm and 562–567 nm, respectively, and a CT-band at 625–628 nm (Figs. 1& S2).

At pH 7.0 the UV–vis bands of the three proteins in the ferric HS state

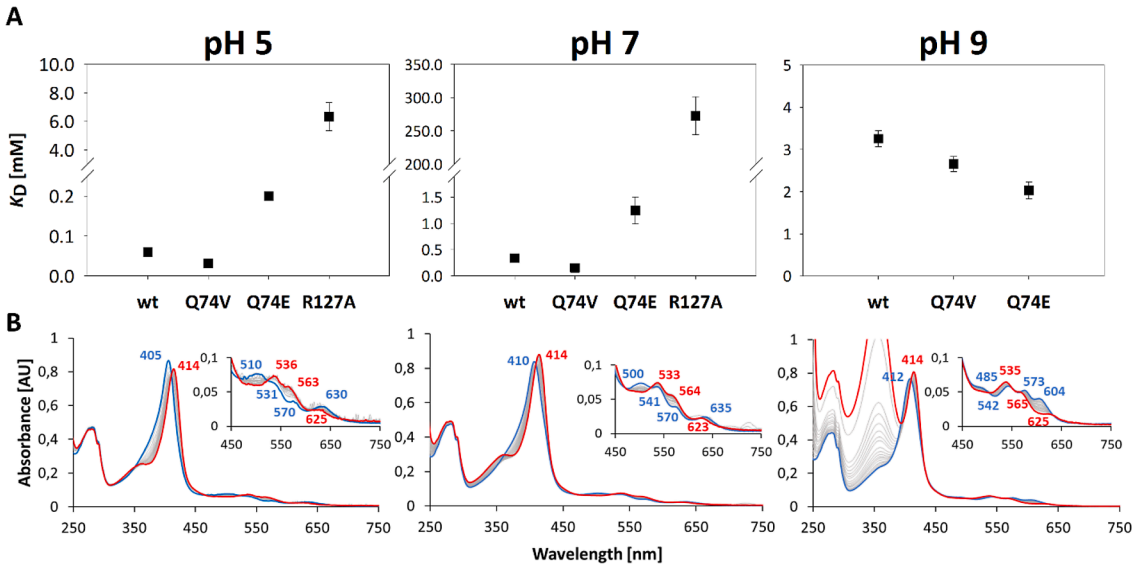

Fig. 1. Formation of nitrite complexes of wild-type chlorite dismutase from *Cyanothece sp.* PCC7425 and the variants Q74V, Q74E and R127A at pH 5.0, 7.0 and 9.0. (A) Dissociation constants (K_D) calculated from thermodynamic titrations followed by UV–vis spectroscopy. (B) Spectral transitions during high-spin (HS) to low-spin (LS) transition of wild-type *C*Cld at pH 5, 7 and 9 (left to right). For Q74V and Q74E see Fig. S2. The insets depict the wavelength range between 450 and 750 nm for better visualization of the Q-bands and CT-bands. Blue spectra represent ferric HS spectra or partially hydroxo-LS spectra, whereas red spectra represent the LS nitrite complexes at the end of titration. A 100- to 3000-fold excess of nitrite was used to obtain the final spectra, for pH 5 and pH 9 respectively. Note that the background absorbance in the UV-region at pH 9.0 derives from the high nitrite concentration that is necessary for formation of a stable nitrite-complex. (For interpretation of the references to colour in this figure legend, the reader is referred to the web version of this article.)

are (slightly) red-shifted (407–410, 533–541, 570–584 and 635 nm). The broad range reflects the differences in alkaline transition reported recently [18]. Similar to pH 5.0, addition of nitrite diminishes the spectral differences between the three proteins and the resulting low-spin spectra exhibit Soret and Q-band maxima at 414, 533–535 and 564–566 nm, respectively (Fig. 1B, Fig. S2). At pH 9.0 all three ferric proteins already exhibit pronounced LS spectral signatures in their resting state (Figs. 1 and S2) and the spectral features of the nitrite complexes were almost identical and similar to those at pH 7.0.

While the UV–vis spectral transitions during conversion of HS to LS states of wild-type *C*Cld and the variants Q74V and Q74E are similar, the calculated K_D-values of the nitrite complexes are varying significantly (Fig. 1A and Table 1) with Q74V showing the highest affinity both at pH 5.0 and 7.0 ($K_D = 31 \pm 2$ μM and $K_D = 153 \pm 41$ μM) followed by wild-type *C*Cld ($K_D = 60 \pm 4$ μM and $K_D = 367 \pm 84$ μM) and Q74E ($K_D = 200 \pm 9$ μM and $K_D = 1250 \pm 250$ μM). At pH 9.0 the affinity of nitrite is low for all three proteins ranging from 2.03 ± 0.2 mM (Q74E) to 3.3 ± 0.2 mM (wild-type *C*Cld).

For R127A and R127K rather different spectral changes are observed upon titration with nitrite (Figs. 2, S2, S3 & S4). In contrast to wild-type *C*Cld and the Q74-variants, the red-shift of bands of ferric R127A during alkaline transition is less pronounced (Figs. S2 and S3). Almost similar bands were observed at pH 5.0 and pH 7.0 (407, 500/501, 545, 639/633 nm), whereas the spectrum at pH 9.0 showed maxima at 409, 533, 564 and 637 nm (Fig. S2). The pH-dependence of the ECD spectra in the Soret region look very similar for wild-type *C*Cld and R127A showing a shift of the Soret band from 414 to 422 nm (wild-type CCld) and 412 to 420 nm (R127A), respectively. In R127K the lysine residue seems to act

Table 1
Calculated dissociation constants for the nitrite complex of wild type CCld and the variants Q74V, Q74E and R127A at pH 5.0, 7.0 and 9.0.

K_D [mM]	pH 5.0	pH 7.0	pH 9.0
wild type	0.060 ± 0.004	0.336 ± 0.084	3.255 ± 0.191
Q74V	0.031 ± 0.002	0.153 ± 0.041	2.657 ± 0.177
Q74E	0.199 ± 0.009	1.246 ± 0.254	2.030 ± 0.204
R127A	6.345 ± 0.994	272.772 ± 28.534	>4000

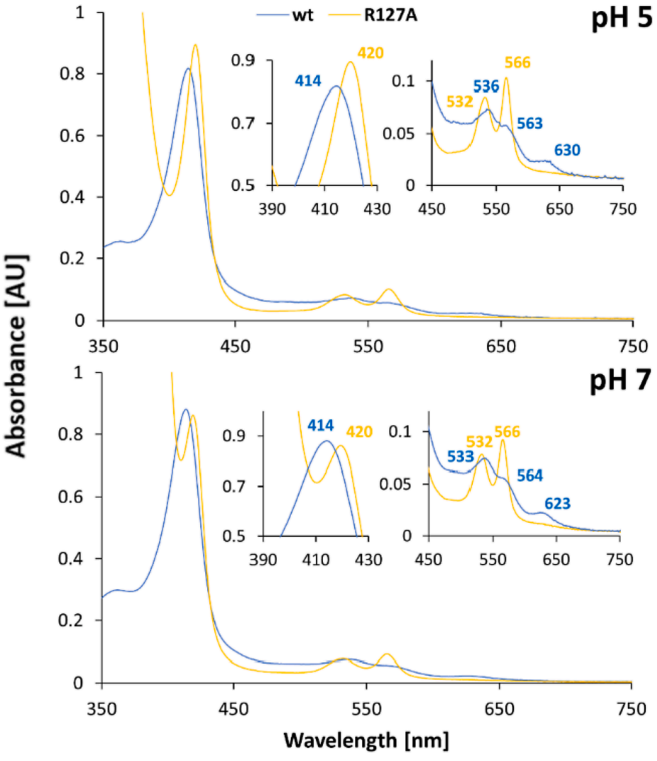

Fig. 2. Comparison of the UV–vis spectra of LS nitrite complexes of wild-type *C*Cld and the variant R127A at pH 5.0 and pH 7.0. For better visualization the two insets depict the Soret region (390–430 nm) and the Q- and CT-band region (450–750 nm) of wild-type *C*Cld (blue) and R127A (yellow). A 100- to 300-fold excess of nitrite was used to obtain the final spectra, for pH 5 and pH 7 respectively. (For interpretation of the references to colour in this figure legend, the reader is referred to the web version of this article.)

as distal heme ligand causing a LS spectrum. At alkaline pH the Soret band is further red-shifted and the Q-bands are sharpened (Fig. S1).

Upon addition of nitrite the resulting Soret maximum of the LS spectrum of R127A was significantly red-shifted compared to that of wild-type *C*Cld, Q74V or Q74E (Fig. 2 and S3). A similar but less significant shift was also seen for R127K at pH 5.0. Here a LS species is already present before addition of nitrite which is caused by the introduced lysine coordinating the heme iron on the distal side (Fig. S4). At both pH 5.0 and pH 7.0 the Soret band of R127A shifted to 420 nm after addition of nitrite, whereas the intensity of the Q-bands at 529 and 567 nm significantly increased and the CT band disappeared (Fig. 2, S2, S3 and S4).

The pronounced difference in spectral signatures of LS species of nitrite complexes between wild-type *C*Cld and R127A is also reflected by the respective visible ECD spectra. For wild-type *C*Cld the Soret maximum moves to 424 nm upon nitrite binding, whereas for both R127A and R127K the corresponding ellipticity maxima shifted to 427 nm (Figs. S4).

Elimination of the distal arginine dramatically reduces the affinity of nitrite. Calculated K_D values of the nitrite complex (Table 1) of R127A vary from 6.4 ± 0.9 mM (pH 5.0), 273 ± 29 mM (pH 7.0) to >4000 mM (pH 9.0). For R127K no reliable K_D values could be calculated. It has to be mentioned that at very high nitrite concentrations formation of nitrogen monoxide and formation of the respective NO-heme complex could occur at acidic and neutral pH which impedes both correct spectral assignment of the respective nitrite complexes of the two R127 variants and reliable calculation of the dissociation constants. This will be discussed later on.

EPR analysis of wild-type *C*Cld and variants in the presence of nitrite reveals the formation of low-spin ferric species with distinct EPR features, corroborating the UV–visible spectroscopy findings. The X-band

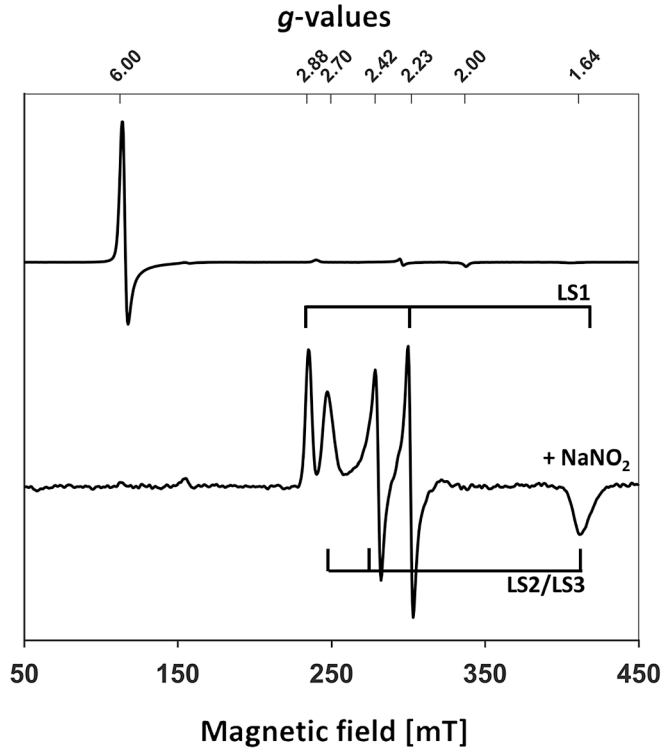

Fig. 3. X-band CW EPR spectra of wild-type *C*Cld (top) and NO_2^--*C*Cld complex (bottom), at neutral pH. Samples were prepared either in 50 mM sodium-phosphate buffer (wild-type CCld) [18] or in 50 mM TIP buffer (NO_2^--*C*Cld complex), pH 7. Measurements were performed with microwave powers of either 2 mW (wild-type *C*Cld) or 5 mW (NO_2^--*C*Cld complex). Spectra are shown normalized to their maximum intensity.

CW EPR spectrum of wild-type *C*Cld at pH 7 has been already shown elsewhere [16,18], however, it is reported in Fig. 3 and Fig. S5 to highlight the changes induced by the addition of nitrite at.

neutral pH. The HS signal of ferric *C*Cld completely converts into new multiple LS contributions, characterized by different *g* anisotropy (simulation parameters reported in Table 2, simulation in Fig. S6a). Among these, LS1 represents the major contribution and it is well distinguishable from LS2 and LS3, which possess rather similar *g*-values and are mostly overlapped. When nitrite is added to the Q74E and Q74V variants at the same pH value (Fig. 4A, B and Fig. S5), the spectrum profile is comparable to the one of wild-type *C*Cld, as the same LS contributions can be detected in similar relative ratios (Table 2, Fig. S6).

Fig. 4C and D depict the EPR spectra of the variants ferric R127A and R127K with and without nitrite at pH 7.0. The exchange of the catalytic arginine to alanine in R127A does not cause dramatic changes in the spectrum, which remains essentially dominated by a high-spin Fe(III) signal (Fig. S7, left panel), although with increased rhombic character (Table S2). On the other hand, the EPR spectrum of R127K is clearly different and dominated by new highly anisotropic low-spin features characterized by very broad and poorly resolved lines, which impede precise estimation of the *g*-values and even the detection of the high-field features (Fig. S7, right panel, Table S2). These spectral features, in accordance with the previously shown UV–vis spectral signatures, indicate that the lysine in the R127K mutant is able to coordinate the heme iron, as demonstrated by the X-ray crystal structure presented below (Fig. 7C).

The EPR spectra of the NO_2^- complexes of R127A and R127K are again dominated by LS species. A signal with similar principal *g*-values to LS1 (therefore referred as LS1*) and a new low-spin species (LS4) contribute almost equally to the spectrum. Notably, in the case of R127A some contribution from the HS signal (9%) remains after the addition of nitrite (Table 2).

In addition, the EPR spectra of wild-type *C*Cld and the variants Q74V and Q74E with nitrite were also measured at pH 8.5, using either a mixture of phosphate and borate buffers or a Tris-HCl buffer (Fig. 5 and S8). The samples were prepared in two different buffers in order to be able to compare the EPR results with other biochemical experiments, where phosphate-based buffers are used, and with the crystal structures, since Tris-HCl buffer is the system used in the crystallization conditions.

In the EPR spectra of nitrite-ligated wild-type *C*Cld all three LS species are retained at high pH, although small differences in relative ratios can be observed, with even a very minor contribution from a OH^--ligated low-spin species [18] noticeable in the sample prepared in Tris-HCl (Fig. 5A and Table 3). Conversely, significant changes occur when the NO_2^- complexes of the Q74E and Q74V variants are prepared at

Table 2
EPR parameters of NO_2^- complexes of wild-type *C*Cld (WT) and variants at pH 7.0 obtained by simulation of the spectra. Simulation of high-spin species were performed both with the *g*-values of an effective $S = ½$ system and the *g*-values of a real $S = 5/2$ system (data not shown); the latter were used to determine % contributions (errors: *g*-values ±0.01, contribution ±1%).

Protein	Species	g_z	g_y	g_x	%
WT	LS1	2.87	2.24	1.64	58
	LS2	2.73	2.40	1.62	29
	LS3	2.69	2.42	1.62	13
Q74E	LS1	2.88	2.23	1.63	59
	LS2	2.74	2.41	1.62	19
	LS3	2.70	2.42	1.62	22
Q74V	LS1	2.88	2.23	1.63	68
	LS2	2.72	2.41	1.62	21
	LS3	2.70	2.43	1.62	11
R127A	HS	1.99	5.61	6.00	9
	LS1*	2.88	2.23	1.58	35
	LS4	2.78	2.38	1.60	56
R127K	LS1*	2.90	2.22	1.57	49
	LS4	2.78	2.38	1.60	51

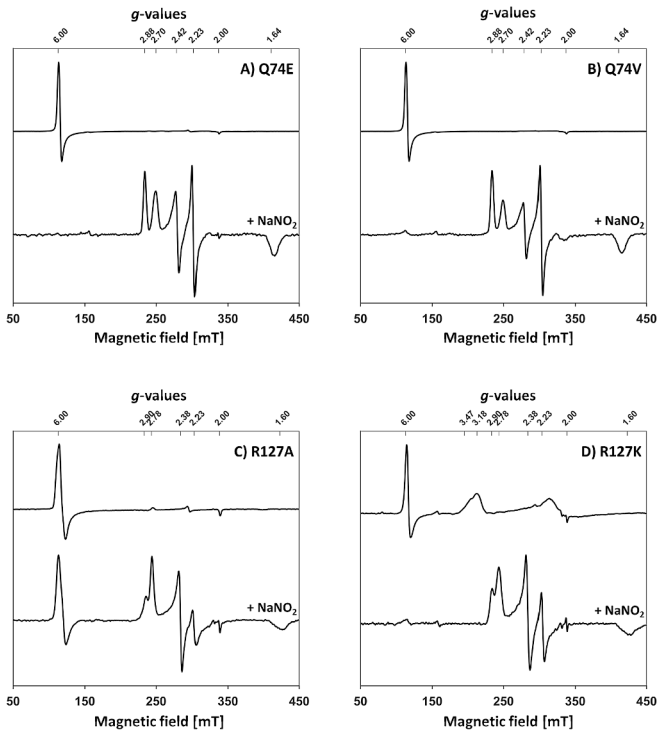

Fig. 4. X-band CW EPR spectra of ferric HS *C*Cld variants and the corresponding LS nitrite adducts (bottom spectra) at pH 7.0. A) Q74E; B) Q74V; C) R127A; D) R127K; Samples were prepared in 50 mM sodium-phosphate buffer, pH 7. Measurements were performed with microwave powers of either 2 mW (resting state of wild-type, Q74 *C*Cld variants and NO_2^--Q74 variants complexes) or 1 mW (resting state of R127 variants and NO_2^--R127 variants complexes). Spectra are shown normalized to their maximum intensity.

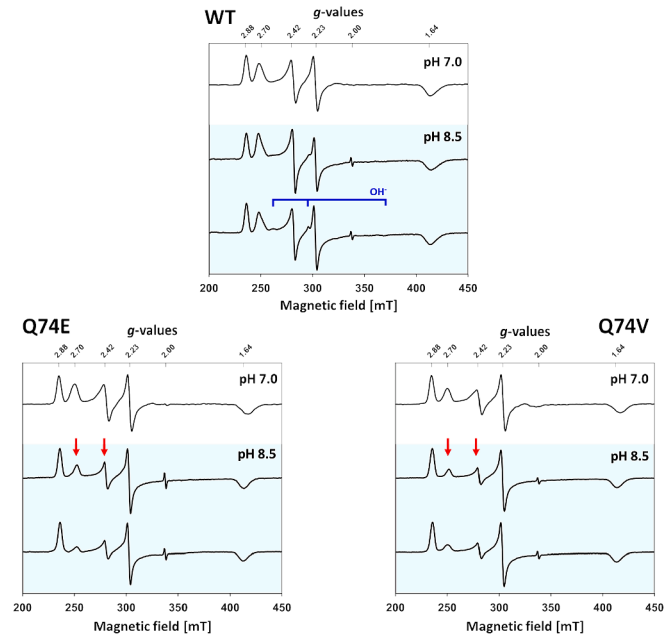

Fig. 5. X-band CW EPR spectra of NO_2^--*C*Cld complexes at different pH values and buffers (low-spin region only). Top: 50 mM sodium-phosphate buffer, pH 7; middle: 50 mM phosphate/borate buffer, pH 8.5; bottom: 50 mM Tris-HCl pH 8.5. The OH^- LS species is highlighted in blue; red arrows indicate the features with most significant changes. Measurements were performed with microwave powers of either 2 mW (NO_2^- complexes pH 7) or 0.6 mW (NO_2^- complexes pH 8.5). Spectra are shown normalized to their maximum intensity. (For interpretation of the references to colour in this figure legend, the reader is referred to the web version of this article.)

alkaline pH. While the LS2 species is no longer detected (as it can be seen by the disappearance of asymmetry in the peaks corresponding to the overlapping LS2/LS3), the EPR contribution from the other species is also altered in favour of LS1, as indicated by the diminished intensity of the g_z and g_y features of LS3 (see red arrows in Fig. 5 and Fig. S8) and by the ratios calculated from simulations (Table 3).

A well-defined predominance of a LS species with *g*-values close to those of LS1 (referred as LS1**) is also observable in the EPR spectrum of the NO_2^- adduct of the clade 1 pentameric chlorite dismutase from "*Candidatus* Nitrospira Defluvii" (*Nd*Cld) [8] at pH 7 that is shown in Fig. S9. Here the addition of nitrite induces the complete disappearance of the rhombic high-spin signal of ferric *Nd*Cld, but it is not sufficient to remove the highly anisotropic low-spin contribution (LS0, Table S3) which dominates the spectrum of *Nd*Cld in absence of the ligand [10,18].

3.2. Chlorite degradation activity and thermal stability of the nitrite complexes of wild-type CCld and the variants Q74V, Q74E, R127A and R127K

It was previously shown that the flexibility of the catalytic R127 has no notable influence on the overall catalytic activity of *C*Cld [18]. The catalytic efficiencies (k_{cat}/K_M) of chlorite degradation of wild-type *C*Cld and the variants Q74V and Q74E are similar. At pH 7.0 the hierarchy of K_M values is Q74V < wild-type *C*Cld < Q74E thereby reflecting the hierarchy of the K_D values of the nitrite adducts. The k_{cat} values decrease in the following order: Q74E > wild-type *C*Cld > Q74V (Table 4).

Exchange of R127 significantly reduces the catalytic efficiency of chlorite degradation. At pH 7.0 for both variants (R127A and R127 K) the k_{cat}/K_M values are decreased by almost 3 orders of magnitude (Table 4) reflected by K_M values in the low mM range and decreased

Table 3
Relative contributions to the EPR spectra of the NO_2^- complexes of wild-type *C*Cld (WT) and the variants Q74E and Q74V at pH 8.5 in different buffers. Principal *g* values are given in Table 2 for LS1, LS2 and LS3. The OH^- species has $g_z = 2.59$, $g_y = 2.28$ and $g_x = 1.83$ (errors: *g* values ±0.01, contribution ±1%).

	Species	%
WT		
Phosphate/borate	LS1	49
	LS2	33
	LS3	17
Tris-HCl	LS1	60
	LS2	25
	LS3	13
	OH^-	2
Q74E		
Phosphate/borate	LS1	75
	LS3	25
Tris-HCl	LS1	80
	LS3	20
Q74V		
Phosphate/borate	LS1	85
	LS3	15
Tris-HCl	LS1	86
	LS3	14

Table 4
Kinetic Parameters of Wild-Type *C*Cld and the Variants Q74V, Q74E, R127A and R127E at pH 7.0.

*C*Cld	K_M (μM)	k_{cat} (s^{-1})	k_{cat}/K_M (M^{-1} s^{-1})
wt[18]	43.2 ± 5.2	60.0 ± 0.7	$1.4 \pm 0.2 \times 10^6$
Q74V[18]	18.8 ± 3.5	50.8 ± 0.4	$2.7 \pm 0.5 \times 10^6$
Q74E[18]	53.8 ± 13.1	37.2 ± 1.1	$6.9 \pm 2.0 \times 10^5$
R127A	2031.0 ± 616.1	3.2 ± 0.1	$1.7 \pm 0.6 \times 10^3$
R127K	2129.5 ± 111.2	10.1 ± 0.4	$4.8 \pm 0.5 \times 10^3$

turnover numbers.

Next, we probed the impact of nitrite binding on the thermal stability of the five heme proteins by differential scanning calorimetry (DSC). As described recently [18], unfolding of *C*Cld follows a non-two state transition reflected by two distinct endotherms (T_m1, T_m2) (Fig. 6). The first unfolding event is reflected by the unfolding of the heme cavity and the release of the prosthetic group, whereas the second transition corresponds to the melting of the overall tertiary fold and the secondary structural elements. In the pH regime 5.0 to 9.0, the second transition (T_m2) is similar for ferric wild-type *C*Cld, Q74V, Q74E and R127A (pH 5: 57.0–58.5 °C; pH 7.0: 62.3–64.3 °C; pH 9.0: 60.0–63.3 °C), whereas R127K exhibits a higher overall stability (pH 5.0: 64.2 °C; pH 7.0: 74.0 °C; pH 9.0: 70.4 °C) (Table S4). By contrast, significant differences are observed in the T_m1 values of the ferric HS proteins. At pH 5.0 and pH 7.0 the order of stability of the heme cavity follows the order Q74E > wild-type *C*Cld > R127K/R127A > Q74V (Table S4).

The impact of nitrite binding on the T_m2 values of the respective LS adducts is relatively small. By contrast, at pH 5.0 the T_m1 values of wild-type *C*Cld, Q74V and R127A are increased by 4.5–6.6 °C, whereas the impact on Q74E and R127K is relatively small (Fig. 6, Table S4). At pH 7.0, nitrite binding to the heme cavity stabilized the active site architecture of wild-type *C*Cld, Q74V and Q74E, whereas no effect is seen with R127A and R127K. At pH 9.0 the impact of nitrite was modest with all proteins (Table S4).

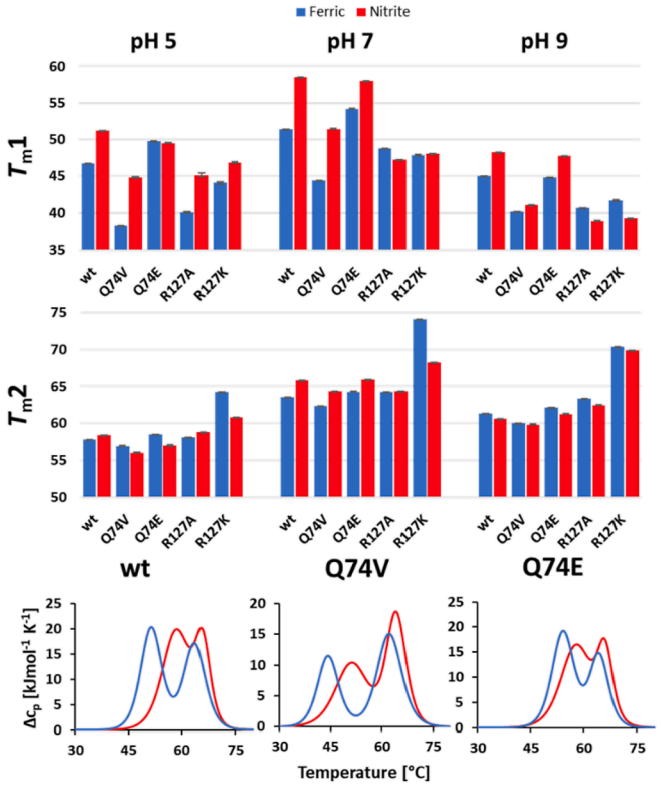

Fig. 6. Thermal stability of unbound HS wild-type *C*Cld and the Q74V, Q74E, R127A and R127K and of the corresponding LS nitrite complexes. (A) Comparison of calculated T_m1 and T_m2 values of in the absence (blue) and presence of nitrite (red) at pH 5.0, 7.0 and 9.0. (B) Representative normalized thermograms of wild-type *C*Cld and the variants Q74V and Q74E at pH 7.0. Enzyme concentration: 20 μM. Measurements were performed in 50 mM citrate phosphate buffer (pH 5.0), 50 mM phosphate buffer (pH 7.0) and 50 mM borate phosphate buffer (pH 9.0). 20 mM, 100 mM and 200 mM of nitrite was added, at pH 5.0, 7.0 and 9.0 respectively. (For interpretation of the references to colour in this figure legend, the reader is referred to the web version of this article.)

3.3. X-ray crystal structures of ferric HS proteins and the corresponding LS nitrite complexes

The X-ray crystal structures of wild-type *C*Cld and the variants Q74V and Q74E have been published recently [17,18]. In addition, structures of ferric wild-type *C*Cld with soaked-in distal ligands (F^- and SCN^-) have been deposited in the PDB [17]. In crystal structures of wild-type *C*Cld (pH 6.5 and pH 8.5) and Q74E (pH 6.5), R127 is present in the "out" conformation, *i.e.* pointing toward the substrate entry channel, whereas in Q74V (pH 8.5) it is pointing toward the heme iron [17,18].

Here, in order to analyse the impact of R127 on binding of the anionic angulate ligand nitrite, which mirrors the substrate chlorite, we have elucidated the crystal structures of the variants R127A and R127K and of the nitrite adducts of wild-type *C*Cld, Q74E, Q74V and R127A, respectively (Table 5). All proteins crystallized either in the space group P1 (R127K and nitrite adducts of wild-type *C*Cld, Q74E and R127A) or $P12_11$ (R127A and nitrite adduct of Q74V). The resolutions of the recorded datasets range from 1.50 Å (nitrite adduct of R127A) to 2.42 Å (nitrite adduct of Q74E) (Table 5). The crystal structures of the homodimeric structures show the typical ferredoxin-like fold that is defined by five α-helices along with a β-barrel composed of three-stranded and five-stranded antiparallel β-sheets [17,18]. The introduced mutations did not lead to significant changes in the overall fold of the *C*Cld variants. If not stated otherwise, both subunits are in good agreement with respect to intramolecular distances and amino acid positions. Therefore, the chain A subunit was used to prepare all figures. Histidine 114 serves as the fifth ligand on the proximal side, with the $N_\varepsilon2$ atom being 1.8–2.4 Å from the heme iron (depending on variant and subunit). In the absence of nitrite, a H_2O molecule is typically situated above the heme iron at a distance of 2.6 Å (wild-type *C*Cld). This water molecule is also visible in 50% of the subunits of the variant R127A, whereas the other subunits showed the presence of the cryoprotectant 2-methyl-2,4-pentanediol (MPD) being bound to the heme iron (Fig. 7A and B). Exchange of R127 by alanine increases the bottleneck radius from 2.2 to 2.8 Å, thereby allowing MPD to enter the active site. In the crystal structure of R127K the lysine acts as sixth heme ligand, thereby eliminating the distal water molecule (Fig. 7C).

Upon addition of nitrite to wild-type *C*Cld, Q74V and Q74E, R127 shows the "in" conformation and interacts with the anionic ligand (Fig. 8A-C). Even in the absence of the catalytic arginine (R127A) a nitrite molecule is visible in the active site and a water molecule takes up the place of the basic amino acid. In some protomers this water molecule is connected by another one with Q74 (Fig. 8D).

In all nitrite-soaked crystals NO_2^- is coordinated to the heme iron *via* an oxygen atom with O-Fe distances ranging from 2.1 to 2.4 Å (Fig. 8). The anionic ligand interacts with the arginine's $N_\eta2$ (2.8 to 3.1 Å) and/or N_ε (2.6 to 2.9 Å), respectively (Fig. 8, Table S5). In R127A a water molecule in a similar position is coordinating one of the oxygens of the bound ligand in a distance of ~3 Å (distances ranging from 2.4 to 3.5 Å). In the LS complexes the direct H-bond between R127 and Q74 is lost. Nevertheless, R127 is hydrogen-bonded to Q74 *via* a water molecule. Together with six additional water molecules, a hydrogen bonding network between $N_\eta1$ and $N_\eta2$ of R127 and $O_\varepsilon1$ of Q74 is visible (Fig. 9). In Q74V the hydrogen bonding network is very similar to that of wild-type *C*Cld. The low resolution of the structure of Q74E does not allow reliable conclusions.

3.4. Molecular dynamic (MD) simulations of active site dynamics

Finally, we probed the dynamics of R127 in ferric HS wild-type *C*Cld, Q74V and Q74E as well as in the respective nitrite complexes by MD simulations. First, we analysed the distance distribution between the heme iron and the C_ζ-atom of R127, as well as the occurrence of H-bonds between R127 and its surrounding residues (Tables 6 and 7) in the absence of nitrite (here the binding site is occupied by a water molecule in all simulations). We performed cluster analysis to determine the most

Table 5
Crystallization Conditions and Data Collection and Refinement Statistics. PDB entries: 7OU5 (wild-type *C*Cld-nitrite complex), 7OU7 (Q74V-nitrite complex), 7OU9 (Q74E-nitrite complex), 7OUY (R127A-nitrite complex), 7OWI (R127A), 7OUA (R127K).

	wt NO_2^-	Q74V NO_2^-	Q74E NO_2^-	R127A NO_2^-	R127A	R127K
PDB-Code	7OU5	7OU7	7OU9	7OUY	7OWI	7OUA
Ligand	NO_2^-	NO_2^-	NO_2^-	NO_2^-	–	–
pH	6.5	8.5	6.5	6.5	8.0	6.5
Wavelength	0.9677	0.9724	0.9724	0.8731	0.9795	0.9795
Resolution range (Å)	29.67–1.90 (1.97–1.90)	47.54–1.63 (1.69–1.63)	45.97–2.42 (2.50–2.42)	28.96–1.50 (1.55–1.50)	44.29–1.70 (1.76–1.70)	40.61–2.09 (2.17–2.09)
Space group	P 1	P 1 21 1	P 1	P 1	P 1 21 1	P 1
Unit cell	51.749 52.759 54.684107.143 98.829109.555	54.954 73.049 59.973 90,112.323 90	52.697 52.684 54.99 98.769107.105109.95	52.25 54.96 93.895 99.508 94.805 98.375	54.447 72.675112.12 90 94.835 90	48.7119 49.6067 54.5788 102.484104.838105.002
Total reflections	134,592 (13867)	107,600 (11129)	31,577 (3224)	500,330 (41325)	649,385 (62390)	84,106 (8591)
Unique reflections	36,350 (3670)	52,809 (5233)	18,659 (1867)	151,776 (13190)	95,807 (9516)	26,289 (2594)
Multiplicity	3.7 (3.8)	2.0 (2.1)	1.7 (1.7)	3.3 (3.1)	6.8 (6.6)	3.2 (3.3)
Completeness (%)	92.15 (93.19)	96.39 (95.84)	96.23 (95.94)	90.79 (64.46)	99.84 (99.87)	83.32 (11.92)
Mean *I*/sigma (*I*)	8.67 (1.75)	14.97 (2.09)	8.10 (3.85)	4.04 (0.40)	14.74 (1.23)	8.90 (0.09)
Wilson B-factor ($Å^2$)	29.16	22.78	33.51	21.41	25.05	58.07
R-merge	0.0874 (0.6726)	0.03428 (0.4666)	0.04882 (0.1726)	0.1384 (2.226)	0.07281 (1.394)	0.07743 (7.039)
R-meas	0.1023 (0.7839)	0.04534 (0.612)	0.06904 (0.2441)	0.1657 (2.679)	0.07893 (1.516)	0.09272 (8.369)
R-pim	0.0529 (0.401)	0.02934 (0.3924)	0.04882 (0.1726)	0.0898 (1.466)	0.03019 (0.5891)	0.05036 (4.482)
CC1/2	0.995 (0.809)	0.998 (0.68)	0.968 (0.928)	0.996 (0.206)	0.999 (0.564)	0.997 (0.376)
CC*	0.999 (0.946)	0.999 (0.9)	0.992 (0.981)	0.999 (0.584)	1 (0.849)	0.999 (0.739)
Reflections used in refinement	36,320 (3667)	52,775 (5233)	18,653 (1867)	147,312 (10429)	95,703 (9510)	22,396 (319)
Reflections used for R-free	951 (96)	851 (85)	953 (97)	1515 (103)	1177 (116)	1679 (28)
R-work	0.1816 (0.3141)	0.1676 (0.2809)	0.1814 (0.1978)	0.2494 (0.4347)	0.1742 (0.3188)	0.2217 (0.4774)
R-free	0.2109 (0.3598)	0.1896 (0.3296)	0.2356 (0.2727)	0.2747 (0.4300)	0.1965 (0.3562)	0.2698 (0.5280)
CC(work)	0.967 (0.881)	0.966 (0.847)	0.932 (0.916)	0.964 (0.542)	0.971 (0.779)	0.952 (0.602)
CC(free)	0.938 (0.664)	0.964 (0.856)	0.901 (0.760)	0.961 (0.595)	0.976 (0.763)	0.905 (0.556)
Number of non-hydrogen atoms	3406	3337	3227	6991	7004	3170
macromolecules	3006	3008	3014	5818	5978	2980
ligands	166	106	189	534	493	299
solvent	297	231	100	878	764	32
Protein residues	364	364	362	704	722	362
rmsd for bonds (Å)	0.011	0.010	0.003	0.007	0.008	0.005
rmsd for angles (deg)	0.96	0.78	0.53	0.75	0.84	0.85
Ramachandran favoured (%)	97.78	98.33	96.93	97.24	98.03	96.37
Ramachandran allowed (%)	2.22	1.67	3.07	2.76	1.97	3.63
Ramachandran outliers (%)	0.00	0.00	0.00	0.00	0.00	0.00
Rotamer outliers (%)	0.00	0.00	0.00	0.17	0.00	0.32
Clashscore	4.38	3.40	2.90	3.38	2.50	7.04
Average B-factor ($Å^2$)	40.76	29.19	40.96	35.44	31.26	66.72
macromolecules	41.07	28.97	41.18	35.02	30.62	67.05
ligands	29.91	20.70	37.13	31.32	28.94	63.83
solvent	41.33	35.71	38.57	39.62	37.06	49.97
Number of TLS groups	6	15	7	20	27	5

Statistics for the highest-resolution shell are shown in parentheses.

common active site architecture(s). In wild-type ferric *C*Cld at least one H-bond is present between R127 and Q74 at all times with the distance between the heme iron and the C_ζ-atom of R127 varying between 6.3 Å and 6.5 Å (Fig. 10, Table 6). This is in good agreement with the crystal structure (6.4 Å) having R127 in the "out" conformation.

Interestingly, neither Q74E nor Q74V show a comparable homogeneous distribution. In the Q74E variant, the salt bridge seen in the crystal structure between R127 and E74 is only present in 10 or 20% of the simulation time (summed up over all H-bonds between arginine's $N_\eta1$ and $N_\eta2$ and the carboxy group of E74) depending on the analysed subunit. Indeed, R127 in Q74E occupies a second distinct conformation where it is flipped out of the active site placing its C_ζ-atom at 8.9 Å distance from the heme iron. Also, in this conformation the guanidium group stays in plane with the heme porphyrin ring (Fig. 10).

In ferric HS Q74V the distance between the C_ζ-atom of R127 in the "out" conformation is slightly higher (6.9 Å) compared to wild-type *C*Cld, most probably because more space is available as valine is smaller. A second conformation places the C_ζ-atom of R127 at 8.9 Å distance to the heme iron. This conformation, however, is distinctly different from Q74E as the guanidinium group is not only shifted but also turned upwards and out of plane with regard to the heme porphyrin ring.

Simulation of the nitrite adducts shows that in the conformation of wild-type *C*Cld R127 is in the "in" conformation (5.4 Å distance). Interestingly, the H-bond between $N_\eta1$ of R127 and Q74 is persistent, whereas the oxoanion is H-bonded to N_ε, and $N_\eta2$ (Table 7). In the

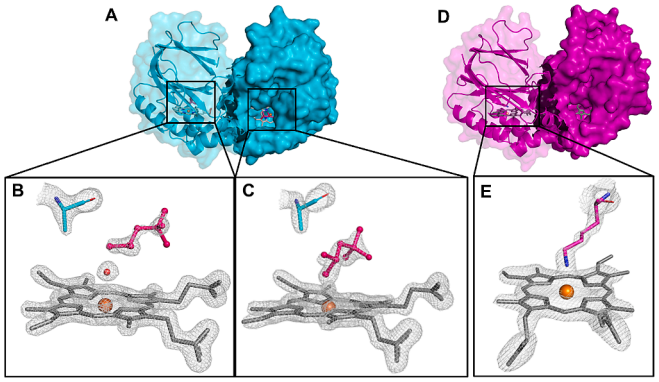

Fig. 7. Crystal structures of the *C*Cld variants R127A (A, B, C, cyan) and R127K (D, E, magenta) with $2F_o$-F_c electron density maps contoured at σ = 1.5. (A) Crystal structure of *C*Cld variant R127A (cyan). One monomer of each dimer is shown in cartoon representation with a transparent surface representation in the background, while the other monomer is depicted in surface representation. The heme *b* cofactor (grey) is shown in stick representation. The heme iron is depicted as an orange sphere, while MPD (burgundy) in the active site is shown in sticks and spheres representation. (B, C) Alanine at position 127 (cyan) is shown in stick representation. In 50% of the monomers MPD is bound to the heme iron. (D) Crystal structure of *C*Cld variant R127K (magenta). One monomer is shown in cartoon representation with a transparent surface representation in the background, while the other monomer is depicted in surface representation. (E) In the variant R127K the lysine residue (magenta) is coordinating the heme iron (orange). $2F_o$-F_c electron density maps (grey meshes) were contoured at σ = 1.5 using PyMOL (http://www.pymol.org/). (For interpretation of the references to colour in this figure legend, the reader is referred to the web version of this article.)

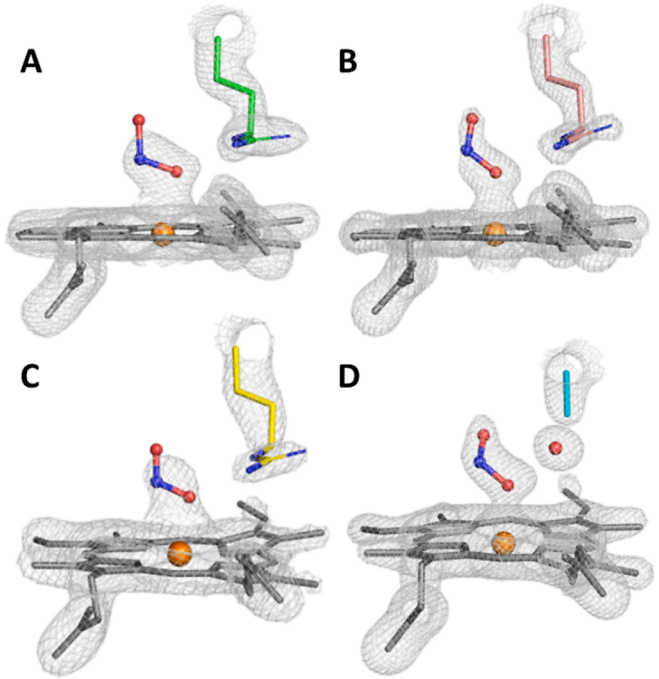

Fig. 8. Crystal structure of distal heme cavity of nitrite adducts of wild-type *C*Cld (A, green), Q74V (B, flamingo), Q74E (C, yellow) and R127A (D, cyan) including the $2F_o$-F_c electron density maps. The amino acid residue at position 127, arginine (in A, B and C) or alanine (in D), and the heme *b* cofactor (grey) are shown in stick representation. The soaked ligand, nitrite (NO_2^-), is shown in stick and sphere representation (blue and red). Relevant water molecules and the heme iron are depicted as red and orange spheres, respectively. $2F_o$-F_c electron density maps (grey meshes) were contoured at σ = 1.5 using PyMOL (http://www.pymol.org/). (For interpretation of the references to colour in this figure legend, the reader is referred to the web version of this article.)

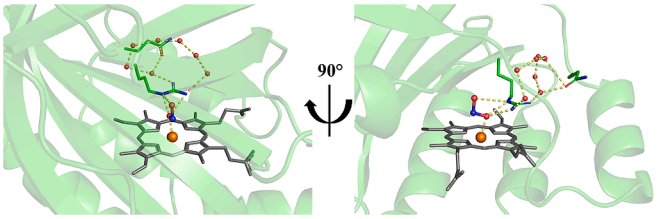

Fig. 9. Hydrogen bonding network of nitrite bound at the active site of wild-type *C*Cld. Details from X-ray crystal structure of nitrite adduct (Fig. 8A). The amino acid residues R127 and Q74 (green) are shown in stick representation. The soaked ligand, nitrite (NO_2^-) is depicted in stick and sphere representation (blue and red). Relevant water molecules and the heme iron are depicted as red and orange spheres, respectively. Hydrogen bonds are indicated by yellow dashed lines. Heme pocket is shown in transparent cartoon representation (green). This figure was generated using PyMOL (http://www.pymol.org/). (For interpretation of the references to colour in this figure legend, the reader is referred to the web version of this article.)

Table 6
Hydrogen bonding pattern of R127 $N_\eta 1$ and R127 $N_\eta 2$ and distal amino acids in the two subunits of ferric wild-type CCld (wt-1, wt-2) and the variants Q74E and Q74V and the corresponding nitrite complexes during 50 ns simulation. Listed are H-bonds which occur with a frequency of more than 1% in the resting state throughout the simulation time (50 ns).

Protein	Subunit	Acceptor	Donor-acceptor atoms	Resting state	NO_2^--bound state
				(frequency in %)	
wt	1	Q74	$N_\eta 1$ -OE1	77.4	92.72
			$N_\eta 2$-OE1	76.4	0.16
	2	Q74	$N_\eta 1$ -OE1	71.9	59.84
			$N\eta_2$-OE1	67.6	0.42
		L70	$N_\eta 1$-O	5.8	0
		V73	$N_\eta 1$-O	5.4	0
Q74E	1	V73	$N_\eta 1$-O	17.4	3.04
		L70	N-OE2	11.9	0
		E74	$N_\eta 1$ -OE1	3.2	19.59
			$N_\eta 1$- OE2	2.0	20.95
			$N_\eta 2$-OE1	2.8	4.35
			$N_\eta 2$ -OE2	1.68	6.57
	2	V73	$N_\eta 1$-O	62.1	0
		L70	$N_\eta 2$-O	56.8	0
		E74	$N_\eta 1$ -OE1	10.0	30.78
			$N_\eta 1$ - OE2	2.9	32.64
			$N_\eta 2$-OE1	6.3	0.36
			$N_\eta 2$ -OE2	1.63	0.09
Q74V	1	Q71	$N_\eta 1$ -OE1	2.2	0
			$N_\eta 2$-OE1	3.0	0
	2	Q71	$N_\eta 2$-OE1	1.26	0
			$N_\eta 1$ -OE1	1.14	0

Table 7
Dynamics of H-bonding pattern between nitrite or chlorite and R127 N_ε and R127$N_\eta 2$ in the two subunits of wild-type *C*Cld (wt-1) and (wt-2) and the variants Q74E and Q74V. Listed are H-bonds which occur with a frequency of more than 1% in the resting state throughout the simulation time (50 ns). Numbers represent % of occurrence.

Donor-Acceptor atom	wt −1	wt −2	Q74E −1	Q74E −2	Q74V -1	Q74V -2
N_ε-O_1 NO_2^-	85.9	82.7	16.5	39.2	90.1	95.6
N_ε-O_2 NO_2^-	84.6	81.2	17.0	31.8	66.4	75.3
$N_\eta 2$-O_1 NO_2^-	42.3	51.9	4.3	18.2	37.1	16.5
$N_\eta 2$-O_2 NO_2^-	57.0	51.6	7.2	43.0	83.7	90.3
N_ε-O_1 ClO_2^-	81.4	93.7	100.0	13.5	13.3	16.7
N_ε-O_2 ClO_2^-	48.4	51.3	16.7	97.8	88.4	99.3
$N_\eta 2$-O_1 ClO_2^-	17.1	51.6	17.0	95.5	40.5	96.3
$N_\eta 2$-O_2 ClO_2^-	4.4	4.8	97.8	21.6	55.1	22.1

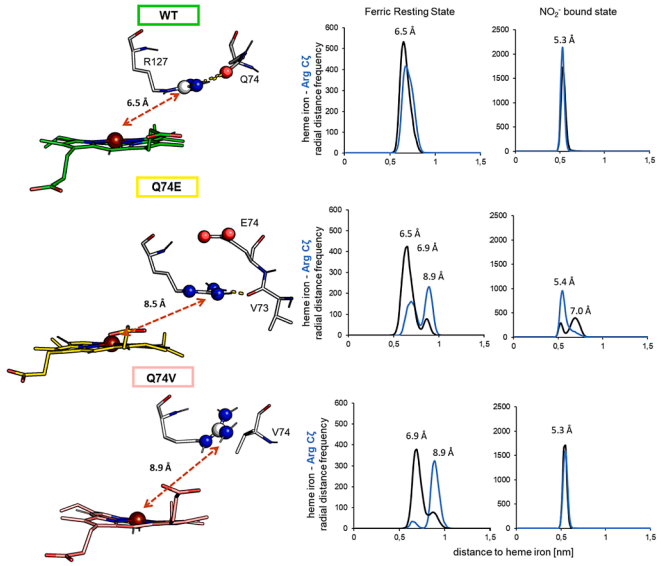

Fig. 10. Dynamics of Arg127 of wild-type *C*Cld and the variants Q74E and Q74V in the HS ferric state and the respective LS nitrite complexes. Left panel: Representative structures. Middle panel: Distance distribution between the ferric HS heme iron and the C_ζ-atom of R127 during simulations. Right panel: Distance distribution between the ferric heme iron in the nitrite complexes and the C_ζ-atom of R127 during simulations. Distance distribution in subunit 1 is depicted in black, distance distribution in subunit 2 in blue. The most dominant distances are labelled. The amino acid residues R127 and Q74/E74/V74 (white) are shown in stick representations, the H-bonds between R127 and Q74 are shown as yellow dashes. The heme cofactor is coloured according to the variant depicted and the distance between the iron and the C_ζ of R127 is illustrated with dashed arrows. This figure was generated using PyMOL (http://www.pymol.org/). (For interpretation of the references to colour in this figure legend, the reader is referred to the web version of this article.)

ligand-bound Q74V variant, the arginine is in the "in" conformation throughout the whole simulation time and interacts with nitrite *via* N_ε, and $N_\eta 2$ (Fig. 11). Interestingly, the nitrite complex of Q74E shows two distinct distances of the C_ζ-atom of R127, namely the "in" conformation (5.4 Å) and an "out" conformation (7.0 Å), where R127 is still in a salt bridge with E74 for at least 30% of the simulation time (Fig. 10). As a consequence, two distinct ligation states of nitrite are observed with NO_2^- either ligated directly above the heme iron (as in wild-type *C*Cld and Q74V) or in a "dragged off" conformation. Importantly, MD

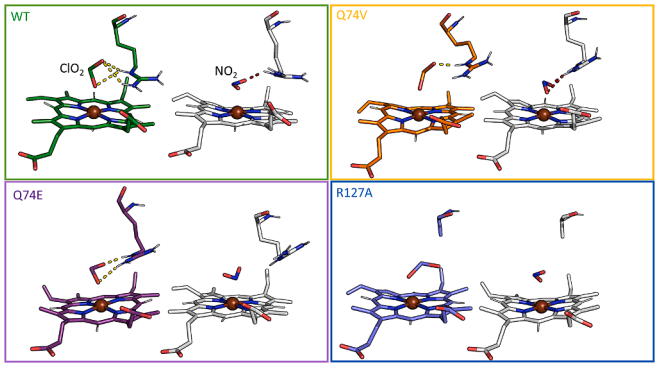

Fig. 11. Comparison of exemplary structures showing chlorite (left) or nitrite (right) bound to wild-type *C*Cld (green) or the variants Q74E (magenta), Q74V (yellow) and R127A (blue) variant. The heme cofactor, the amino acid residues and the ligands are shown as stick representation. Hydrogen bonds between chlorite/nitrite and R127 are shown when present (Yellow = chlorite, firebrick = nitrite). (For interpretation of the references to colour in this figure legend, the reader is referred to the web version of this article.)

simulations of the nitrite complexes suggest that besides dominating *O*-ligation, also ligand binding *via* a nitrogen atom could occur (Fig. 11). In Q74E *N*-ligation is seen more frequently than in Q74V. Tables 6 and 7 summarize the differences between the ferric states and the corresponding nitrite-bound states in the H-bonding pattern between R127 and nitrite, as well as R127 and distal amino acids including L70, V73 and Q74 (wild-type *C*Cld) or E74 (Q74E) as well as Q71 (Q74V).

Next, we analysed the dynamics of chlorite binding to wild-type *C*Cld and the variants Q74V and Q74E. MD simulations suggest that if chlorite is bound in the active site it is positioned in a more upright manner compared to nitrite which adopts a conformation more plane parallel with the heme (Fig. 11). With nitrite, both *O*- and *N*-coordination of the heme iron are observed whereas with chlorite exclusively *O*-ligation is found. Table 7 depicts the differences in dynamics of H-bonding between R127 and the low-spin ligands nitrite and chlorite. Chlorite is continuously hydrogen-bonded to R127 in wild-type *C*Cld with H-bonds present between R127 N_ε and one or both chlorite oxygen atoms, while the H-bond between R127 $N_\eta 2$ and the oxygen atoms of chlorite appears significantly less often when compared to nitrite. In the variant Q74E, where the H-bonding network between nitrite and R127 was found to be significantly weaker (~ 16–30% for N_ε and 4–40% for $N_\eta 2$ of the simulation time) compared to wild-type *C*Cld, two H-bonds between R127 and the chlorite O-atoms are present throughout the whole simulation, one including N_ε and one $N_\eta 2$ of R127. Only in the variant Q74V, where H-bonds between nitrite and R127 are present throughout the whole simulation time, the H-bonding between chlorite and R127 is similar to nitrite. The average distance between the chlorine atom of chlorite and the heme iron is 3.5 Å compared to 3 Å distance between the nitrogen atom of nitrite and the heme iron, reflecting the vertical *versus* planar ligation.

4. Discussion

Catalysis mediated by heme enzymes may involve (among others) the basic amino acid arginine. Often, this arginine can adopt different conformations in the heme cavity within a reaction cycle and thus can influence the reactivity of distinct enzyme intermediates in different ways. This also applies in particular to the enzyme chlorite dismutase, which has only one catalytic amino acid in the distal hydrophobic heme cavity, namely a fully conserved and flexible arginine. It has been shown by both X-ray and neutron crystallography that this conserved distal arginine R127 in wild-type ferric *C*Cld is positioned away from the heme moiety at pH 6.5, 8.5 and pH 9.0 [17]. This "out" conformation is stabilized by hydrogen bonding between $N_\eta 1$ of R127 and $O_\varepsilon 1$ of Q74 [17]. Recently, we have probed the impact of modulation of this non-covalent interaction by exchanging of Q74 by valine or glutamate. Our findings clearly demonstrated that (i) the distal arginine in wild-type Clds is flexible, (ii) its dynamics is influenced by its remote H-bonding partner, and (iii) in Q74V this flexibility is more pronounced than in wild-type *C*Cld, whereas in Q74E, R127 is arrested in a salt-bridge with Q74E [18]. The hierarchy in flexibility of R127 (Q74V > wild-type *C*Cld > Q74E) was nicely reflected by the pK_a values of the alkaline transition, *i.e.* the deprotonation of the distal ligand water W501: 7.41 (Q74V), 8.11 (wild-type *C*Cld) and 9.33 (Q74E) [18]. This is supported by the fact that in the crystal structure of Q74V at pH 8.5 R127 is in the "in" conformation and interacts with (deprotonated) W501 *via* H-bonds to $N_\eta 2$ and N_ε [18] The series of pK_a values underlines the impact of the positively charged R127 and its dynamics in stabilizing the conjugate base of distal water. The transition of HS to LS ferric wild-type *C*Cld and Q74V and Q74E at higher pH through formation of a hydroxide-ligated ferric heme form was confirmed by both UV–vis and EPR spectroscopies [18].

Moreover, the differences in the conformational dynamics of R127 has also a strong impact on the thermal stability of the heme cavity. The respective $T_m 1$ values increase in the following order: Q74V (38.3 °C) < wild-type *C*Cld (45.8 °C) < Q74E (50.9 °C) (Fig. 6) [18]. The higher thermal stability of Q74E in the resting state derives from the salt bridge

of R127 with E74, which is located at the (flexible) α-helical loop that connects the N-terminal and C-terminal ferredoxin-like domains of *C*Cld protomers [18]. However, MD simulations suggest also that E74 is not fully arrested in this salt bridge, but is able to visit a second conformation that establishes an H-bond with the backbone, which resembles the situation in clade 1 Clds. In general, ligation of nitrite at the distal heme position further increases the thermal stability of the resulting LS complex heme cavity architecture. The importance of R127 in stabilization of the nitrite complexes is underlined by the fact that addition of nitrite to R127A has no impact on the thermal stability (Fig. 6). Here, it has to be mentioned that a very high nitrite concentrations nitrite is known to form nitrogen monoxide at acidic and neutral pH regimes, which might impede correct data interpretation since the resulting NO-complexes have different spectral signatures and complex stabilities compared to the nitrite complexes [49].

Further, at the pH optimum and neutral pH, the K_M values (derived from kinetic chlorite degradation data) decrease in the following order: Q74E > wild-type *C*Cld > Q74V (Table 4), which mirrors the hierarchy of the (i) thermal stability of the heme cavity, (ii) of the pK_a values of the alkaline transition and (iii) of the K_D values of the nitrite complexes. In the absence of the catalytic arginine, both chlorite and nitrite are still able to bind to the heme iron and mediate the HS to LS transition, but the resulting low-spin complexes of *C*Cld are extremely unstable. This clearly underlines the importance of R127 in stabilizing both the substrate adduct (Reaction 1) and the nitrite complex (Reaction 2). The higher the flexibility of R127, the higher is its stabilizing effect on the respective complexes. At pH optimum and neutral pH, Q74V shows the highest affinity for both chlorite and nitrite, followed by wild-type *C*Cld and Q74E. The K_D values (nitrite) significantly increase with increasing pH suggesting that the interaction between R127 and the nitrite is impaired at alkaline pH. This is supported by the fact that addition of nitrite to wild-type *C*Cld as well as to Q74V and Q74E at pH 9.0 has no impact on the thermal stability compared to pH optimum or neutral pH.

In contrast to the published fluoride and thiocyanate complexes of *C*Cld, where R127 is in the "out" conformation [17], the crystal structures of the nitrite complexes of wild-type *C*Cld, Q74V and Q74E show R127 in the "in" conformation (Figs. 7-9) suggesting that the anionic distal ligand offers energetically more favourable interactions for the guanidinium group compared to the H-bond between R127 with Q74 in the ferric HS wild-type *C*Cld or even the salt-bridge between R127 and E74 in the variant Q74E. This is supported by the UV–vis data that suggest similar solution structures of the nitrite adducts of wild-type *C*Cld, Q74V and Q74E (Figs. 1, S2, S3). The pronounced differences seen in the respective absorption spectra of the three proteins in their HS ferric resting state are in large part diminished upon addition of the anionic ligand between pH 5.0 and pH 7.0.

The crystal structures of wild-type *C*Cld suggest that nitrite is coordinated to the heme iron *via* an oxygen with O-Fe distances ranging from 2.1 to 2.4 Å. The two oxygen atoms of the ligand are hydrogen bonded to $N_\eta 2$ and/or N_ε of the arginine. At least one H-bond is always established during the whole simulation period and a water molecule directly bridges R127 with Q74 in the wild-type *C*Cld-nitrite complex. The water molecule is part of an extended H-bonding network at the distal heme side (Fig. 9). The important role of R127 in keeping nitrite in place is clearly underlined by the significant differences in spectral signatures between R127A and wild-type *C*Cld (as well as Q74V and Q74E) (Figs. 2, S3, S4).

MD simulations show differences in the molecular dynamics of the respective nitrite complexes and offer an explanation for the enhanced K_D and K_M values observed in Q74E. In the nitrite and chlorite complex of this variant, R127 can adopt two conformations and as a consequence two binding *modi* for nitrite are observed. This seems to have a more pronounced effect on k_{off} than on k_{on} and could explain the increased K_D value of the nitrite complex of this variant. Moreover, MD simulations show that *N*-ligation of nitrite is also possible. This agrees with the EPR data, which also clearly show the presence of multiple low-spin species in the spectra of the NO_2^- ligated proteins. These can be attributed to the presence of both *O*- and *N*- ligation. All the NO_2^- adducts investigated in this work show at least two well-resolved contributions from low-spin ferric heme species in their X-band CW-EPR spectra (Figs. 3-5, S5, S6, S8, S9, Tables 2, 3). The appearance of multiple LS signals in the EPR spectra of heme proteins upon addition of nitrite has been extensively described [50–54]. These observations have been attributed either to nitrite linkage isomerism [51], different ligand orientations in distinct subunits [54], heme ruffling (*e.g.,* distortions outside the porphyrin plane) or variations in the extended H-bonding network both at the proximal and the distal side of the heme iron [52,53].

We propose that the different LS contributions in the EPR spectra of NO_2^--Clds complexes might represent the binding of the ligand *via* either *O*-linkage or *N*-linkage. To support this hypothesis, an analysis of the crystal-field parameters using Taylor's formalism for ferric low-spin heme complexes was performed [21,24]. The parameters, calculated for each LS contribution according to equations [1 – 3] (see Materials and Methods), are reported in Table S6 and were used to construct the "Blumberg-Peisach" diagram depicted in Fig. S12 [25], which has been used in the past to classify different iron ligation patterns. In this case, the LS species clearly fall into two distinct clusters. LS1 and the closely related LS1* and LS1** form a compact group with predominant tetragonal character characterized by $\Delta/\lambda \sim 4$ and $V/\Delta \sim 0.5$, while LS2, LS3 and LS4 constitute a more heterogeneous set with $2.35 \leq \Delta/\lambda \leq 2.70$ and $0.86 \leq V/\Delta \leq 1.09$. The only low-spin species formed when nitrite is added to the model heme protein myoglobin at pH 7 (Fig. S10) has *g*-values and crystal-field parameters similar to LS1, falling therefore in the same cluster. In fact, the EPR parameters found for the NO_2^--Mb complex are consistent with the ones reported in previous studies on globins [51,54,55]. Interestingly, it has been shown that both myoglobin and hemoglobin coordinate the nitrite anion with a *O*-nitrito mode [56,57]. In globins this mode of binding is promoted by the presence of a H-bond donor residue at the distal side of the heme iron, a role that in Clds could be likely played by the catalytic arginine. In particular, as shown by Yi et al., in the H64V/V67R double mutant of myoglobin a rearrangement of the mutated arginine sidechain toward the nitrite anion is observed [58], which is reminiscent of the conformational switch described for the catalytic arginine in chlorite dismutases turnover [5–9,11–18]. The attribution of the LS1 cluster to the *O*-linkage binding mode is also consistent with previous findings on clade I chlorite dismutases. A spectroscopic investigation of the hexameric chlorite dismutase from *A. orizae* (*Ao*Cld) in presence of nitrite showed the formation of a low-spin species (*g*-values = [2.93 2.18 1.55]) with very similar features to the LS1** of *Nd*Cld (Fig. S9 and Table S3) [59]. Later, the crystal structure of the nitrite complex of the pentameric (clade 1) chlorite dismutase from *Dryobalanops aromatica* (*Da*Cld) was published, revealing a coordination of nitrite to the heme iron through *O*-linkage [5]. Additional low-spin components, namely LS2 (LS2** for *Nd*Cld), LS3 and LS4, have remarkably similar *g*-values to the ones of nitrite adducts of some heme *b*-containing proteins from the class of nitrophorins. Indeed, a low-spin species with *g*-values = ~ [2.7 2.4 1.5] was identified as the major contribution in the CW-EPR spectra of these proteins, however, other signals from LS with higher *g*-anisotropy were observed as well [52,53]. Among the known isoforms of nitrophorins, NP4 has been crystallized in presence of nitrite, showing a N-nitro coordination mode. It is therefore tempting to attribute the signals from LS2, LS3 and LS4 in chlorite dismutases to the coordination of nitrite *via* the nitrogen atom.

Particularly interesting is that even in the absence of the catalytic arginine (R127A and R127K) the features of a nitrite adduct are clearly distinguishable in the EPR spectra (Fig. 4C, D and Fig. S5). The residual high-spin signal in the spectrum of the NO_2^- complex of R127A (Fig. 4C) reflects the very low affinity of nitrite for this mutant. In the case of R127K, the highly anisotropic low-spin features present in the unbound protein (Fig. 4D top and S7, right panel) are assigned to the coordination of the heme iron by the lysine residue replacing the catalytic arginine, in

accordance with UV–vis findings (Fig. S3) and crystal structure (Fig. 7C). The *g*-values of these contributions (Table S2) are consistent with the ones reported for lysine coordination in other heme systems [60–63]. It has to be noted that due to the high pK_a of Lys (~ 10.5), its binding to the heme iron should be unfavoured at neutral pH. On the other hand, the ferric heme iron is a strong Lewis-acidic species that significantly decreases the pK_a values of protic ligands. Nonetheless, it has been reported that lysine can act as a distal ligand in particular heme systems, giving rise to a mixture of penta- and hexacoordinate heme iron, both in its reduced and oxidized states [64]. The factors responsible for Lys-Fe stabilization have been shown to be related to specific interactions established either between the side-chains of (polar) residues found in the heme proximity or between the heme propionate groups and the protein moiety [65]. In the case of Cld, such polar and anionic interactions need to be excluded, given the hydrophobic character of the heme pocket. Similarly, a change in local pH, which could explain the deprotonation of lysine, appears unlikely, since the UV–vis and EPR spectra of alkaline Clds show clear differences from the Lys-coordinated form [18]. Therefore, the determinants of lysine coordination in chlorite dismutases remain to be elucidated. Nonetheless, the *g*-values of LS-b (Table S2), which is the main low-spin contribution in the R127K variant, are remarkably similar to those of the highly anisotropic LS species found in *Nd*Cld both at acidic/neutral and basic pH values (LS0, see Table S3 & Fig. S9) [18]. This would suggest a similar nature of the distal ligand and a possible coordination by the catalytic arginine in *Nd*Cld, provided that particular factors could allow a suitable protonation state of this residue at low pH. However, this hypothesis is purely speculative to date.

Interestingly, while LS0 in *Nd*Cld persists in the nitrite-adduct of the same enzyme to some extent (Table S3, Fig. S9), from the EPR spectra of the NO_2^- complex of R127K it is evident that nitrite is able to displace the lysine, at least when present in high excess, since the low-spin features of the unbound enzyme are replaced by LS1* and LS4 (Fig. 4D, bottom and Fig. S5). Finally, in R127A and R127K the *N*-linkage binding mode could be favoured by the absence of a H-bond donor residue, in line with what was stated above. This is also supported by the increased contribution of LS4 in the EPR spectra (Fig. 4C, D, Fig. S5 and Table 2). Although all the crystal structures of the available NO_2^--*C*Cld complexes (Figs. 7-9) show a nitrite molecule bound to the heme iron through *O*-linkage, it is possible that only one mode of coordination is stable enough to be resolved under the crystallization conditions. On the other side, the EPR of frozen samples might be considered as a more representative "snapshot" of a natural state in which less favoured binding modes can occur as well, without excluding that cryogenic conditions may also favour states that are less populated at higher temperatures.

5. Conclusions

In summary, it has been demonstrated that the flexibility of the catalytic arginine of clade II chlorite dismutases has a strong impact on the thermodynamics of binding of the angulate oxoanions nitrite and chlorite. At pH optimum (*i.e.*, pH 5.5) and neutral pH the K_D value for nitrite and the K_M value for chlorite are lowest when R127 is highly flexible and highest when R127 exhibits a salt bridge with E74. Upon ligand binding this salt bridge is broken and, similar to wild-type *C*Cld and Q74V, R127 forms two H-bonds with nitrite that is mainly *O*-ligated to the heme iron. Nevertheless, multiple binding *modi* of nitrite are suggested by both MD-simulations and EPR spectroscopy. By contrast, MD simulations demonstrate that chlorite is always *O*-ligated and interacts with R127 in a slightly different manner compared to nitrite. In the absence of the catalytic arginine both oxoanions are still able to bind, but the resulting low-spin ferric heme complexes are extremely unstable as reflected by significantly increased K_D and K_M values. A pronounced increase in K_M has also been observed in the R183A variant of clade 1 Cld from *Dechloromonas aromatica* [11], whereas the effect was smaller with clade 1 Cld from *Nd*Cld [12]. Importantly, the K_D value of nitrite significantly increases with increasing pH and differences within variants with modulated H-bonding network of the catalytic arginine (Q74V, Q74E) disappear at pH values higher than 8.5. The spectroscopic data clearly suggest structural rearrangements in the heme cavity at alkaline pH that could be responsible for the decrease in affinity of the oxoanions. In any case, this suggests that the thermodynamics of substrate binding, *i.e.,* substrate adduct formation, might contribute to shaping the overall pH-dependence of chlorite degradation.

Immediately after substrate binding *via O*-ligation to Fe(III) and concomitant establishment of H-bonds between the two oxygen atoms of chlorite with R127 in the "in"-conformation, the redox reaction takes place and chlorite is converted to chloride and dioxygen. During Reactions 3 and 4 the catalytic R127 most probably stays in the "in" conformation and keeps the transient (oxidizing and chlorinating) intermediates (hypochlorite or chlorine monoxide) in the reaction sphere in order to avoid oxidative damage of the protein matrix and the prosthetic group [14,66]. However, this implies dynamic rearrangements of the original hydrogen bonds, which are established in Compound I or Compound II. After (heterolytic or homolytic) cleavage of chlorite, migration and rotation of the intermediates (hypochlorite or chlorine monoxide), the rebound step and molecular oxygen formation take place with both oxygen atoms being H-bonded with R127 as suggested by a density-functional theory (DFT) study [63]. Finally, to facilitate the departure of the chloride anion, the hydrogen bonds between R127 and the two oxygen atoms are required to rearrange again to the terminal negatively charged chloride [66]. The present data suggest that at pH < 7 the impact of the flexibility of R127 on Reactions 3 and 4 is small. However, at alkaline pH - due to structural rearrangement of the distal H-bonding network – the function of R127 as dynamic H-bonding partner seems to be impaired and the catalytic efficiency significantly decreases. Transient oxidizing intermediates are released from the reaction sphere and as a consequence the level of irreversible inhibition increases with increasing pH as observed in all Clds studied so far [14,15].

Accession codes

Cld from *Cyanothece* sp. PCC7425 (*C*Cld), UniProt entry B8HNS6, PDB entry 5MAU.

Funding

This work was supported by the European Union's Horizon 2020 research and innovation programme under the Marie Skłodowska-Curie grant agreement,European Union [grant number 813209] and the Austrian Science Foundation (FWF), Austria [Doctoral program BioToP – Molecular Technology of Proteins (W1224) and the projects P30979 and I2429]. Funding organizations had no involvement in the conducted research and subsequent preparation of this article.

Declaration of Competing Interest

The authors declare that they have no known competing financial interests or personal relationships that could have appeared to influence the work reported in this paper.

Acknowledgements

The DSC equipment was kindly provided by the EQ-BOKU VIBT GmbH and the BOKU Core Facility for Biomolecular & Cellular Analysis. The authors would like to acknowledge the use of *Servicio General de Apoyo a la Investigación-SAI, Universidad de Zaragoza*. Moreover, the authors would like to thank Diamond Light Source for beamtime (proposal mx20221), and the staff of beamlines I04 for assistance with the data collection. Furthermore, beamtime was granted by the MX2195 proposal (beamlines ID23-1, ID23-2 and ID30A-3) at European

Synchrotron Radiation Facility (ESRF), Grenoble, France.

Appendix A. Supplementary data

Supplementary data to this article can be found online at https://doi.org/10.1016/j.jinorgbio.2021.111689.

References

[1] S. Hofbauer, I. Schaffner, P.G. Furtmüller, C. Obinger, Chlorite dismutases - a heme enzyme family for use in bioremediation and generation of molecular oxygen, Biotechnol. J. 9 (2014) 461–473.

[2] I. Schaffner, S. Hofbauer, M. Krutzler, K.F. Pirker, P.G. Furtmüller, C. Obinger, Mechanism of chlorite degradation to chloride and dioxygen by the enzyme chlorite dismutase, Arch. Biochem. Biophys. 574 (2015) 18–26.

[3] B. Goblirsch, R.C. Kurker, B.R. Streit, C.M. Wilmot, J.L. Dubois, Chlorite dismutases, DyPs, and EfeB: 3 microbial heme enzyme families comprise the CDE structural superfamily, J. Mol. Biol. 408 (2011) 379–398.

[4] S. Hofbauer, V. Pfanzagl, H. Michlits, D. Schmidt, C. Obinger, P.G. Furtmüller, Understanding molecular enzymology of porphyrin-binding α + β barrel proteins - one fold, multiple functions, Biochim. Biophys. Acta - Proteins Proteomics 1869 (2021) 140536.

[5] D.C. de Geus, E.A.J. Thomassen, P.L. Hagedoorn, N.S. Pannu, E. van Duijn, J. P. Abrahams, Crystal structure of chlorite dismutase, a detoxifying enzyme producing molecular oxygen, J. Mol. Biol. 387 (2009) 192–206.

[6] B.R. Goblirsch, B.R. Streit, J.L. DuBois, C.M. Wilmot, Structural features promoting dioxygen production by *Dechloromonas aromatica* chlorite dismutase, J. Biol. Inorg. Chem. 15 (2010) 879–888.

[7] B.R. Streit, B. Blanc, G.S. Lukat-Rodgers, K.R. Rodgers, J.L. DuBois, How active-site protonation state influences the reactivity and ligation of the heme in chlorite dismutase, J. Am. Chem. Soc. 132 (2010) 5711–5724.

[8] J. Kostan, B. Sjöblom, F. Maixner, G. Mlynek, P.G. Furtmüller, C. Obinger, M. Wagner, H. Daims, K. Djinović-Carugo, Structural and functional characterisation of the chlorite dismutase from the nitrite-oxidizing bacterium "*Candidatus* Nitrospira defluvii": identification of a catalytically important amino acid residue, J. Struct. Biol. 172 (2010) 331–342.

[9] G. Mlynek, B. Sjöblom, J. Kostan, S. Füreder, F. Maixner, K. Gysel, P.G. Furtmüller, C. Obinger, M. Wagner, H. Daims, K. Djinović-Carugo, Unexpected diversity of chlorite dismutases: a catalytically efficient dimeric enzyme from *Nitrobacter winogradskyi*, J. Bacteriol. 193 (2011) 2408–2417.

[10] S. Hofbauer, M. Bellei, A. Sündermann, K.F. Pirker, A. Hagmüller, G. Mlynek, J. Kostan, H. Daims, P.G. Furtmüller, K. Djinović-Carugo, C. Oostenbrink, G. Battistuzzi, C. Obinger, Redox thermodynamics of high-spin and low-spin forms of chlorite dismutases with diverse subunit and oligomeric structures, Biochemistry 51 (2012) 9501–9512.

[11] B. Blanc, J.A. Mayfield, C.A. McDonald, G.S. Lukat-Rodgers, K.R. Rodgers, J. L. DuBois, Understanding how the distal environment directs reactivity in chlorite dismutase: spectroscopy and reactivity of Arg183 mutants, Biochemistry 51 (2012) 1895–1910.

[12] S. Hofbauer, K. Gysel, M. Bellei, A. Hagmüller, I. Schaffner, G. Mlynek, J. Kostan, K.F. Pirker, H. Daims, P.G. Furtmüller, G. Battistuzzi, K. Djinović-Carugo, C. Obinger, Manipulating conserved heme cavity residues of chlorite dismutase: effect on structure, redox chemistry, and reactivity, Biochemistry 53 (2014) 77–89.

[13] A. Sündermann, M.M. Reif, S. Hofbauer, C. Obinger, C. Oostenbrink, Investigation of ion binding in chlorite dismutases by means of molecular dynamics simulations, Biochemistry 53 (2014) 4869–4879.

[14] S. Hofbauer, C. Gruber, K.F. Pirker, A. Sündermann, I. Schaffner, C. Jakopitsch, C. Oostenbrink, P.G. Furtmüller, C. Obinger, Transiently produced hypochlorite is responsible for the irreversible inhibition of chlorite dismutase, Biochemistry 53 (2014) 3145–3157.

[15] A.I. Celis, Z. Geeraerts, D. Ngmenterebo, M.M. Machovina, R.C. Kurker, K. Rajakumar, A. Ivancich, K.R. Rodgers, G.S. Lukat-Rodgers, J.L. Dubois, A dimeric chlorite dismutase exhibits O_2-generating activity and acts as a chlorite antioxidant in *Klebsiella pneumoniae* MGH 78578, Biochemistry. 54 (2015) 434–446.

[16] I. Schaffner, S. Hofbauer, M. Krutzler, K.F. Pirker, M. Bellei, G. Stadlmayr, G. Mlynek, K. Djinovic-Carugo, G. Battistuzzi, P.G. Furtmüller, H. Daims, C. Obinger, Dimeric chlorite dismutase from the nitrogen-fixing cyanobacterium *Cyanothece* sp. PCC7425, Mol. Microbiol. 96 (2015) 1053–1068.

[17] I. Schaffner, G. Mlynek, N. Flego, D. Pühringer, J. Libiseller-Egger, L. Coates, S. Hofbauer, M. Bellei, P.G. Furtmüller, G. Battistuzzi, G. Smulevich, K. Djinović-Carugo, C. Obinger, Molecular mechanism of enzymatic chlorite detoxification: insights from structural and kinetic studies, ACS Catal. 7 (2017) 7962–7976.

[18] D. Schmidt, I. Serra, G. Mlynek, V. Pfanzagl, S. Hofbauer, P.G. Furtmüller, K. Djinović-Carugo, S. Van Doorslaer, C. Obinger, Arresting the catalytic arginine in chlorite dismutases: impact on heme coordination, thermal stability, and catalysis, Biochemistry 60 (2021) 621–634.

[19] N. Le Breton, J.J. Wright, A.J.Y. Jones, E. Salvadori, H.R. Bridges, J. Hirst, M. M. Roessler, Using hyperfine electron paramagnetic resonance spectroscopy to define the proton-coupled electron transfer reaction at Fe-S cluster N_2 in respiratory complex I, J. Am. Chem. Soc. 139 (2017) 16319–16326.

[20] S. Stoll, A. Schweiger, EasySpin, a comprehensive software package for spectral simulation and analysis in EPR, J. Magn. Reson. 178 (2006) 42–55.

[21] B.J.S. Griffith, L.E. Orgel, Ligand-field theory, Q. Rev. Chem. Soc. 11 (1957) 381–393.

[22] G. Zoppellaro, K.L. Bren, A.A. Ensign, E. Harbitz, R. Kaur, H.P. Hersleth, U. Ryde, L. Hederstedt, K.K. Andersson, Review: studies of ferric heme proteins with highly anisotropic/highly axial low spin ($S = 1/2$) electron paramagnetic resonance signals with bis-histidine and histidine-methionine axial iron coordination, Biopolymers 91 (2009) 1064–1082.

[23] P.J. Alonso, J.I. Martínez, I. García-Rubio, The study of the ground state Kramers doublet of low-spin heminic system revisited. A comprehensive description of the EPR and Mössbauer spectra, Coord. Chem. Rev. 251 (2007) 12–24.

[24] C.P.S. Taylor, The EPR of low spin heme complexes relation of the τ2g hole model to the directional properties of the g tensor, and a new method for calculating the ligand field parameters, Biochim, Biophys Acta - Protein Struct. 491 (1977) 137–148.

[25] W.E. Blumberg, J. Peisach, Low-spin compounds of heme proteins, ACS Adv. Chem. (1971) 271–291.

[26] C. Jakopitsch, K.F. Pirker, J. Flemmig, S. Hofbauer, D. Schlorke, P.G. Furtmüller, J. Arnhold, C. Obinger, Mechanism of reaction of chlorite with mammalian heme peroxidases, J. Inorg. Biochem. 135 (2014) 10–19.

[27] W. Kabsch, XDS, Acta Crystallogr. Sect. D: Biol. Crystallogr. 66 (2010) 125–132.

[28] P.A. Karplus, K. Diederichs, Linking crystallographic model and data quality, Science 336 (2012) 1030–1033.

[29] A.J. McCoy, R.W. Grosse-Kunstleve, P.D. Adams, M.D. Winn, L.C. Storoni, R. J. Read, Phaser crystallographic software, J. Appl. Crystallogr. 40 (2007) 658–674.

[30] P. Emsley, B. Lohkamp, W.G. Scott, K. Cowtan, Features and development of Coot, Acta Crystallogr. Sect. D: Biol. Crystallogr. 66 (2010) 486–501.

[31] P.D. Adams, P.V. Afonine, G. Bunkóczi, V.B. Chen, I.W. Davis, N. Echols, J. J. Headd, L.W. Hung, G.J. Kapral, R.W. Grosse-Kunstleve, A.J. McCoy, N. W. Moriarty, R. Oeffner, R.J. Read, D.C. Richardson, J.S. Richardson, T. C. Terwilliger, P.H. Zwart, PHENIX: a comprehensive Python-based system for macromolecular structure solution, Acta Crystallogr. Sect. D: Biol. Crystallogr. 66 (2010) 213–221.

[32] S. French, K. Wilson, On the treatment of negative intensity observations, Acta Crystallogr. Sect. A: Cryst. Phys., Diffr Theor. Gen. Crystallogr. 34 (1978) 517–525.

[33] E.A. Merritt, To B or not to B: a question of resolution? Acta Crystallogr. Sect. D: Biol. Crystallogr. 68 (2012) 468–477.

[34] A. Bacchi, V.S. Lamzin, K.S. Wilson, A self-validation technique for protein structure refinement: the extended Hamilton test, Acta Crystallogr. Sect. D: Biol. Crystallogr. 52 (1996) 641–646.

[35] W.C. Hamilton, Significance tests on the crystallographic R factor, Acta Crystallogr. 18 (1965) 502–510.

[36] R.P. Joosten, J. Salzemann, V. Bloch, H. Stockinger, A.C. Berglund, C. Blanchet, E. Bongcam-Rudloff, C. Combet, A.L. Da Costa, G. Deleage, M. Diarena, R. Fabbretti, G. Fettahi, V. Flegel, A. Gisel, V. Kasam, T. Kervinen, E. Korpelainen, K. Mattila, M. Pagni, M. Reichstadt, V. Breton, I.J. Tickle, G. Vriend, PDB-REDO: automated re-refinement of X-ray structure models in the PDB, J. Appl. Crystallogr. 42 (2009) 376–384.

[37] I.W. Davis, L.W. Murray, J.S. Richardson, D.C. Richardson, MolProbity: structure validation and all-atom contact analysis for nucleic acids and their complexes, Nucleic Acids Res. 32 (2004) W615–W619.

[38] J. Stourac, O. Vavra, P. Kokkonen, J. Filipovic, G. Pinto, J. Brezovsky, J. Damborsky, D. Bednar, Caver web 1.0: identification of tunnels and channels in proteins and analysis of ligand transport, Nucleic Acids Res. 47 (2019) W414–W422.

[39] N. Schmid, C.D. Christ, M. Christen, A.P. Eichenberger, W.F. van Gunsteren, Architecture, implementation and parallelisation of the GROMOS software for biomolecular simulation, Comput. Phys. Commun. 183 (2012) 890–903.

[40] M.M. Reif, M. Winger, C. Oostenbrink, Testing of the GROMOS force-field parameter set 54A8: structural properties of electrolyte solutions, lipid bilayers, and proteins, J. Chem. Theory Comp. 9 (2013) 1247–1264.

[41] C. Zou, M. Larisika, G. Nagy, J. Srajer, C. Oostenbrink, X. Chen, W. Knoll, B. Liedberg, C. Nowak, Two-dimensional heterospectral correlation analysis of the redox-induced conformational transition in cytochrome c using surface-enhanced Raman and infrared absorption spectroscopies on a two-layer gold surface, J. Phys. Chem. 117 (2013) 9606–9614.

[42] D.H.J. Mackay, A.J. Cross, A.T. Hagler, The role of energy minimization in simulation strategies of biomolecular systems, in: G.D. Fasman (Ed.), Prediction of Protein Structure and the Principles of Protein Conformation, Springer, 1989, pp. 317–358.

[43] H.J.C. Berendsen, J.P.M. Postma, W.F.V. Gunsteren, J.T. Hermans, Interaction models for water in relation to protein hydration, in: B. Pullman (Ed.), Intermolecular Forces, D. Reidel Publishing Company, Dordrecht, 1981, pp. 331–342.

[44] H.J.C. Berendsen, J.P.M. Postma, W.F. Van Gunsteren, A. Dinola, J.R. Haak, Molecular dynamics with coupling to an external bath, J. Chem. Phys. 81 (1984) 3684–3690.

[45] J.P. Ryckaert, G. Ciccotti, H.J.C. Berendsen, Numerical integration of the cartesian equations of motion of a system with constraints: molecular dynamics of n-alkanes, J. Comput. Phys. 23 (1977) 327–341.

[46] H.J.C. Berendsen, W.F. Van Gunsteren, H.R.J. Zwinderman, R.G. Geurtsen, Simulations of proteins in water, Ann. NY Acad. Sci (1986) 269–286.

[47] I.G. Tironi, R. Sperb, P.E. Smith, W.F. Van Gunsteren, A generalized reaction field method for molecular dynamics simulations, J. Chem. Phys. 102 (1995) 5451–5459.

[48] T.N. Heinz, W.F. Van Gunsteren, P.H. Hünenberger, Comparison of four methods to compute the dielectric permittivity of liquids from molecular dynamics simulations, J. Chem. Phys. 115 (2001) 1125–1136.
[49] J.O. Lundberg, E. Weitzberg, M.T. Gladwin, The nitrate-nitrite-nitric oxide pathway in physiology and therapeutics, Nat. Rev. Drug Discov. 7 (2008) 156–167.
[50] L.J. Young, L.M. Siegel, On the reaction of ferric heme proteins with nitrite and sulfite, Biochemistry 27 (1988) 2790–2800.
[51] R. Silaghi-Dumitrescu, D.A. Svistunenko, D. Cioloboc, C. Bischin, F. Scurtu, C. E. Cooper, Nitrite binding to globins: linkage isomerism. EPR silence and reductive chemistry, Nitric Oxide Biol. Chem. 42 (2014) 32–39.
[52] C. He, H. Ogata, M. Knipp, Formation of the complex of nitrite with the ferriheme b β-barrel proteins nitrophorin 4 and nitrophorin 7, Biochemistry 49 (2010) 5841–5851.
[53] C. He, H. Ogata, W. Lubitz, Elucidation of the heme active site electronic structure affecting the unprecedented nitrite dismutase activity of the ferriheme *b* proteins, the nitrophorins, Chem. Sci. 7 (2016) 5332–5340.
[54] B.I. Goetz, H.W. Shields, S. Basu, P. Wang, S.B. King, N. Hogg, M.T. Gladwin, D. B. Kim-Shapiroa, An electron paramagnetic resonance study of the affinity of nitrite for methemoglobin, Nitric Oxide Biol. Chem. 22 (2010) 149–154.
[55] D.E. Schwab, J.S. Stamler, D.J. Singel, EPR spectroscopy of nitrite complexes of methemoglobin, Inorg. Chem. 49 (2010) 6330–6337.
[56] J. Yi, M.K. Safo, G.B. Richter-Addo, The nitrite anion binds to human hemoglobin via the uncommon O-nitrito mode, Biochemistry 47 (2008) 8247–8249.
[57] D.M. Copeland, A.S. Soares, A.H. West, G.B. Richter-Addo, Crystal structures of the nitrite and nitric oxide complexes of horse heart myoglobin, J. Inorg. Biochem. 100 (2006) 1413–1425.
[58] J. Yi, M.K. Safo, G.B. Richter-Addo, The nitrite anion binds to human hemoglobin via the uncommon *O*-nitrito mode, Biochemistry 47 (2008) 8247–8249.
[59] P.L. Hagedoorn, D.C. De Geus, W.R. Hagen, Spectroscopic characterization and ligand-binding properties of chlorite dismutase from the chlorate respiring bacterial strain GR-1, Eur. J. Biochem. 269 (2002) 4905–4911.
[60] M. Ubbink, A.P. Campos, M. Teixeira, N.I. Hunt, H.A.O. Hill, G.W. Canters, Characterization of mutant Met100Lys of cytochrome c-550 from Thiobacillus versutus with lysine-histidine heme ligation, Biochemistry 33 (1994) 10051–10059.
[61] D.L. Brautigan, B.A. Feinberg, B.M. Hoffman, E. Margoliash, J. Peisach, W. E. Blumberg, Multiple low spin forms of the cytochrome c ferrihemochrome, J. Biol. Chem. 252 (1977) 574–582.
[62] G.G. Silkstone, C.E. Cooper, D. Svistunenko, M.T. Wilson, EPR and optical spectroscopic studies of Met80X mutants of yeast ferricytochrome *c*. models for intermediates in the alkaline transition, J. Am. Chem. Soc. 127 (2005) 92–99.
[63] F.I. Rosell, J.C. Ferrer, A.G. Mauk, Proton-linked protein conformational switching: definition of the alkaline conformational transition of yeast iso-1-ferricytochrome *c*, J. Am. Chem. Soc. 120 (1998) 11234–11245.
[64] E.A. Johnson, M.M. Russo, D.B. Nye, J.L. Schlessman, J.T.J. Lecomte, Lysine as a heme iron ligand: a property common to three truncated hemoglobins from Chlamydomonas reinhardtii, Biochim. Biophys. Acta, Gen. Subj. 1862 (12) (2018) 2660–2673.
[65] J.E. Martinez Grundman, Plana L. Julió, J.L. Schlessman, L. Capece, D.A. Estrin, J. T.J. Lecomte, Control of distal lysine coordination in a monomeric hemoglobin: a role for heme peripheral interactions, J. Inorg. Biochem. 219 (2021) 111437.
[66] S. Sun, Z.-S. Li, S.-L. Chen, A dominant homolytic O–cl bond cleavage with low-spin triplet-state Fe(IV)=O formed is revealed in the mechanism of heme-dependent chlorite dismutase, Dalton Trans. 43 (2014) 973–981.